National Renewable Energy Laboratory
A national laboratory of the U.S. Department of Energy
Office of Energy Efficiency & Renewable Energy
Innovation for Our Energy Future

Transport, Interfaces, and Modeling in Amorphous Silicon Based Solar Cells

Final Technical Report
11 February 2002 – 30 September 2006

E.A. Schiff
Syracuse University
Syracuse, New York

Subcontract Report
NREL/SR-520-44101
October 2008

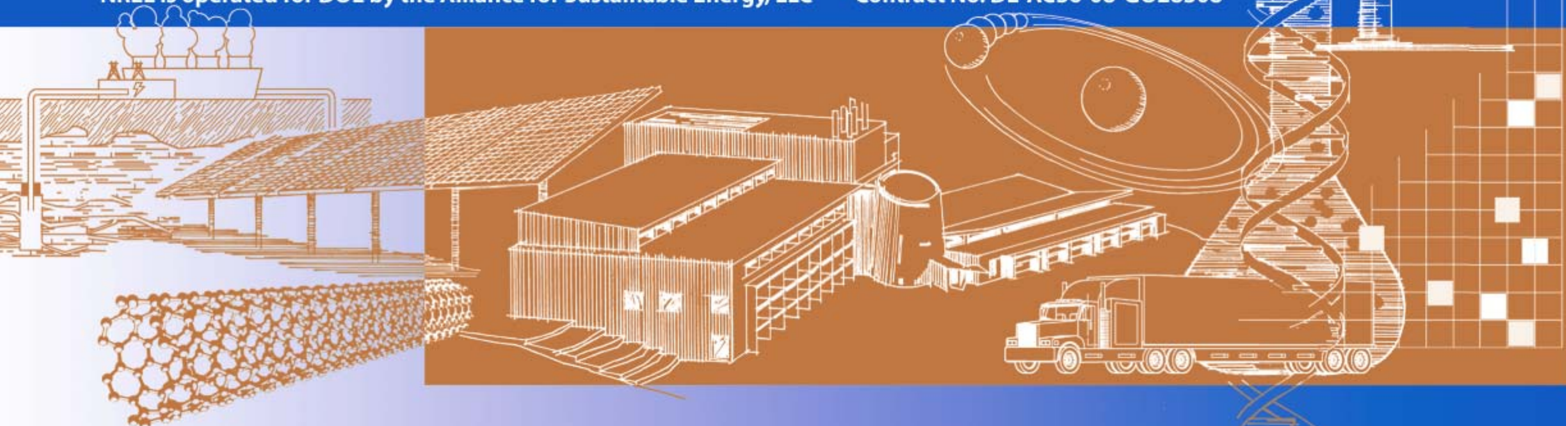

NREL is operated for DOE by the Alliance for Sustainable Energy, LLC
Contract No. DE-AC36-08-GO28308

Transport, Interfaces, and Modeling in Amorphous Silicon Based Solar Cells

Final Technical Report
11 February 2002 – 30 September 2006

E.A. Schiff
Syracuse University
Syracuse, New York

NREL Technical Monitor: Bolko von Roedern
Prepared under Subcontract No. NDJ-2-30630-24

Subcontract Report
NREL/SR-520-44101
October 2008

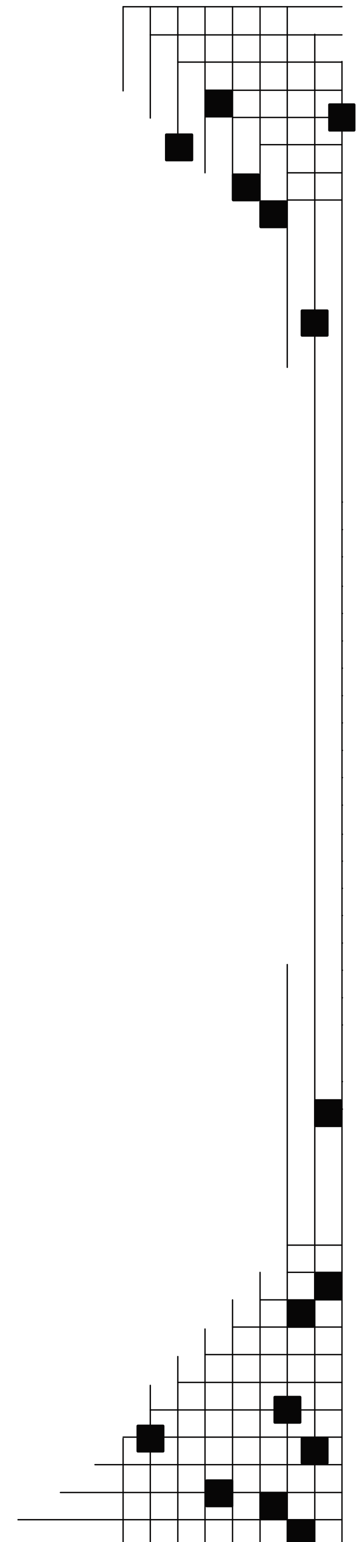

National Renewable Energy Laboratory
1617 Cole Boulevard, Golden, Colorado 80401-3393
303-275-3000 • www.nrel.gov

NREL is a national laboratory of the U.S. Department of Energy
Office of Energy Efficiency and Renewable Energy
Operated by the Alliance for Sustainable Energy, LLC

Contract No. DE-AC36-08-GO28308

This publication was reproduced from the best available copy
Submitted by the subcontractor and received no editorial review at NREL

NOTICE

This report was prepared as an account of work sponsored by an agency of the United States government. Neither the United States government nor any agency thereof, nor any of their employees, makes any warranty, express or implied, or assumes any legal liability or responsibility for the accuracy, completeness, or usefulness of any information, apparatus, product, or process disclosed, or represents that its use would not infringe privately owned rights. Reference herein to any specific commercial product, process, or service by trade name, trademark, manufacturer, or otherwise does not necessarily constitute or imply its endorsement, recommendation, or favoring by the United States government or any agency thereof. The views and opinions of authors expressed herein do not necessarily state or reflect those of the United States government or any agency thereof.

Available electronically at http://www.osti.gov/bridge

Available for a processing fee to U.S. Department of Energy
and its contractors, in paper, from:
U.S. Department of Energy
Office of Scientific and Technical Information
P.O. Box 62
Oak Ridge, TN 37831-0062
phone: 865.576.8401
fax: 865.576.5728
email: mailto:reports@adonis.osti.gov

Available for sale to the public, in paper, from:
U.S. Department of Commerce
National Technical Information Service
5285 Port Royal Road
Springfield, VA 22161
phone: 800.553.6847
fax: 703.605.6900
email: orders@ntis.fedworld.gov
online ordering: http://www.ntis.gov/ordering.htm

Printed on paper containing at least 50% wastepaper, including 20% postconsumer waste

TABLE OF CONTENTS

Summary iv
Solar Cell Characteristics & Modeling iv
Drift Mobility Measurements on CIGS v
Drift Mobility Measurements on Microcrystalline Silicon v
Polymer *p*-layers vi
Optical Properties of n/i and p/i Interfaces vii
A. Characterization & Modeling of a-Si:H Solar Cells 1
1. Introduction 1
2. Hole-mobility Limit for *pin* Solar Cells 1
3. Hole Drift-Mobilities in a-Si:H 3
4. Amorphous Silicon *nip* Solar Cells: Solar Illumination 4
5. Amorphous Silicon Solar Cells: Uniformly Absorbed Illumination 6
6. Light-Soaking Kinetics of the Open-Circuit Voltage 9
B. Hole Drift Mobility Measurements in $CuIn_{1-x}Ga_xSe_2$ Solar Cells 14
1. Introduction 14
2. Specimens 14
3. Time-of-Flight Instrumentation 15
4. Capacitance Measurements 16
5. Transient photocharge measurements 16
6. Transit Time and Drift Mobility Estimates 17
7. Summary of Mobility Measurements 18
8. Discussion 19
9. Appendices 20
C. Hole Drift-Mobility Measurements and Multiple-Trapping in Microcrystalline Silicon 22
1. Introduction 22
2. Samples 23
3. Drift-Mobilities 23
4. Multiple-Trapping Fits 23
5. Meaning of Multiple Trapping in microcrystalline silicon 25
D. Polyaniline heterojunction diodes 27
1. Introduction 27
2. Experimental procedures 27
3. Results and discussion 27
4. Conclusions 30
E. Infrared Interface Spectra in Cells 31
References 35

Summary

In this report we present the results for the four principal tasks of this research project:

1. Amorphous Silicon Solar Cell Characteristics and Modeling
2. Photocarrier Drift Mobility Measurements in hydrogenated amorphous silicon (a-Si:H), microcrystalline silicon (μc-Si:H), and polycrystalline copper indium-gallium diselenide (CIGS).
3. Hole-Conducting Polymers as *p*-layer Materials for Amorphous and Crystal Silicon Solar Cells
4. Infrared spectra of *p/i* and *n/i* interfaces in a-Si:H based solar cells.

We have published thirteen papers, including four in *Applied Physics Letters*, which acknowledge the support from this subcontract. See the references [1- 13] and the associated web-links at the end of this report.

Solar Cell Characteristics & Modeling

The most important finding of our work is that the efficiency of contemporary a-Si:H solar cells is largely governed by the hole drift-mobility; the appropriate exceptions and details are summarized below. This finding is certainly surprising in the context of the field's longstanding focus on dangling bonds as the limitation. Much of this report will be a summary of the experiments which led to this finding, but we first take the liberty of discussing its implications for further improving the efficiency of a-Si:H based solar cells.

There is an interesting "desert" between the best values of the hole drift mobility in a-Si:H (hole drift mobility about 10^{-2} cm^2/Vs) and in nc-Si:H (hole drift-mobility about 10^0 cm^2/Vs); in both a-Si:H and nc-Si:H, the valence bandtails associated with disorder are the root cause of the low hole mobilities compared to crystalline silicon. It seems likely that a-Si:H materials can be grown in this desert that would permit better initial-state solar cells than at present. It is also fairly clear that such materials are not readily achieved. The "triode" materials prepared a decade ago at ETL have never been reproduced, and are the only occupants of the desert known to us.

Presuming that better initial-state cells can be fabricated by optimizing the hole drift-mobility further, would these cells have better efficiencies following light soaking? As will be described below, we believe that light-soaking in a-Si:H is "self-limiting" in contemporary materials. By this phrase, we are suggesting the perspective that dangling bond creation under solar illumination is arrested once dangling bonds become significant competitors to the valence bandtail as photocarrier recombination centers. This hypothesis is certainly not tested as rigorously as our findings regarding the initial-state efficiency. Nonetheless, it implies that materials with improved hole drift mobilities would possess improved properties in their light-soaked state.

What would be the use of such "improved" materials, if indeed they can be created? Presuming that the optical properties of a-Si:H were unchanged, improved electronic properties simply mean that the layer thickness of a-Si:H within the solar cell could be usefully increased. This capability would probably not improve current triple-junction cells, for which the a-SiGe:H layers are the critical ones. We don't presently know whether the ideas of mobility-limitation and self-limitation of light-soaking are valid for a-SiGe:H. On the other hand, improved a-Si:H cells could be quite valuable in "micromorph" and other tandem cell designs, which require thicker component cells and use larger photocurrent densities.

By way of introduction, we now list the principal findings of our work on United Solar Ovonic Corp. single-junction a-Si:H solar cells:

(i) The hole drift mobility is the main electronic property of a-Si:H that determines the power density P_{max} of as-deposited cells [1,2]. Electron drift-mobilities are larger, and nearly irrelevant to the cell's performance. Remarkably, the parameters describing recombination processes are fairly unimportant –

even though recombination is the ultimate fate of photocarriers that don't contribute to power generation. Recombination parameters weakly affect the cell's efficiency through its open-circuit voltage.

(ii) Dangling bonds, which could certainly have reduced the power density below the hole-mobility limit, do not appear to have a strong effect on the as-deposited properties of the cells under solar illumination.

(iii) The power density from light-soaked cells is (of course) noticeably reduced below the as-deposited values. In agreement with previous work, we find that the fairly modest decrease in power is primarily due to the increase of the dangling bond density with light-soaking. However, the photocarrier processes in the light-soaked cells appear to be roughly equally affected by the low hole mobility and by the dangling bond density; the dangling bonds don't dominate the light-soaked state for cells under solar illumination [2,9].

(iv) The time-dependence of light-soaking for the open-circuit voltage is consistent with a reasonable extension of the "hydrogen-collision" model, and appears to be inconsistent with the older approach (often associated with Stutzmann, Jackson, and Tsai) that attributes the time-dependences to changes in photoconductivity kinetics as light-soaking advances [8].

Published work from this task:

"Hole Mobilities and the Physics of Amorphous Silicon Solar Cells," E. A. Schiff, *J. Non-Cryst. Solids* **352**, 1087-1092 (2006).

"Hole Mobility Limit of Amorphous Silicon Solar Cells," Jianjun Liang, E. A. Schiff, Baojie Yan, J. Yang, *Appl. Phys. Lett.* **88** 063512 (2006).

"Light-soaking Effects on the Open-circuit Voltage of Amorphous Silicon Solar Cells," J. Liang, E. A. Schiff, S. Guha, B. Yan, and J. Yang, in *Amorphous and Nanocrystalline Silicon Science and Technology – 2005*, edited by R. Collins, P.C. Taylor, M. Kondo, R. Carius, R. Biswas (Materials Research Society Symposium Proceedings Vol. 862, Pittsburgh, 2005), A13.6.

"Temperature-dependent Open-circuit Voltage Measurements and Light-soaking in Hydrogenated Amorphous Silicon Solar Cells," J. Liang, E. A. Schiff, S. Guha, B. Yan, and J. Yang, in *Amorphous and Nanocrystalline Silicon Science and Technology – 2005*, edited by R. Collins, P.C. Taylor, M. Kondo, R. Carius, R. Biswas (Materials Research Society Symposium Proceedings Vol. 862, Pittsburgh, 2005), A21.8.

"Low Mobility Solar Cells: A Device Physics Primer with Application to Amorphous Silicon," E. A. Schiff, *Solar Energy Materials and Solar Cells* **78**, 567-595 (2003).

Drift Mobility Measurements on CIGS

We have been able to estimate the hole drift-mobility in CIGS using photocarrier time-of-flight methods. For cells prepared by the Noufi's group at NREL, the hole drift-mobility has the magnitude 10^{-1} cm^2/Vs, and is not strongly temperature-dependent. For cells prepared by Bill Shafarman and his colleagues at the Institute of Energy Conversion (IEC), the drift-mobilities are markedly higher, but also exhibit deep-trapping effects that were not seen for the NREL cells. This latter work is an interesting complement to that of Dave Cohen's group, which measured hole mobilities using capacitance methods in IEC samples. Photocarrier time-of-flight measures mobilities in the relatively insulating, front portion of the cell. The capacitance techniques developed by Cohen's group measure hole mobilities in the back portion of the cell , and found a magnitude of 10^1 cm^2/Vs. We suspect the difference is due to vertical inhomogeneities in the CIGS materials of the cell, but this needs to be confirmed.

Drift Mobility Measurements on Microcrystalline Silicon

Our measurements of hole drift mobilities in microcrystalline silicon solar cells from Forschunszentrum Jülich were published in *Applied Physics Letters* [5]. We found that the hole drift-mobility was about 1 cm^2/Vs near room-temperature. The value is much larger than found in amorphous silicon, and it accounts

for the fact that the optimum thickness of microcrystalline solar cells (using the same hole-mobility limited picture just described for a-Si:H cells) is substantially larger than for amorphous silicon.

In three different papers, we have reviewed the overall picture for hole and electron drift-mobilities in amorphous and microcrystalline silicon [1,10]. One interesting result is that the "world champion" hole drift-mobility values are presently reported for "polymorphous" a-Si:H [1]. The physics of the mobility of microcrystalline silicon is also quite interesting. It is unsurprising that the width of the valence bandtail trap distribution for microcrystalline silicon (about 30 meV) is smaller than for a-Si:H (about 45 meV). It is intriguing that the fundamental hole band mobility is about the same for the two materials. And it is surprising that the attempt-to-escape frequency governing emission from the bandtail is much lower for microcrystalline silicon than for amorphous silicon.

Published work from this task:

"Hole Drift Mobility Measurements in Microcrystalline Silicon," T. Dylla, F. Finger, and E. A. Schiff, *Appl. Phys. Lett.* 87, 032103 (2005).

"Drift-mobility measurements and mobility-edges in disordered silicons," E. A. Schiff, *J. Phys.: Condens. Matter* **16**, S5265-5275 (2004).

"Hole Drift-Mobility Measurements and Multiple-Trapping in Microcrystalline Silicon," T. Dylla, F. Finger, and E. A. Schiff, in *Amorphous and Nanocrystalline Silicon Science and Technology – 2004*, edited by G. Ganguly, M. Kondo, E. A. Schiff, R. Carius, and R. Biswas (Materials Research Society, Symposium Proc. Vol. 808, 2004), 109--114.

"Hole Drift-Mobility Measurements in Contemporary Amorphous Silicon," S. Dinca, G. Ganguly, Z. Lu, E. A. Schiff, V. Vlahos, C. R. Wronski, Q. Yuan, in *Amorphous and Nanocrystalline Silicon Based Films - 2003*, edited by J.R. Abelson, G. Ganguly, H. Matsumura, J. Robertson, E. A. Schiff (Materials Research Society Symposium Proceedings Vol. 762, Pittsburgh, 2003), pp. 345--350.

Polymer *p*-layers

Hole conducting polymers are an interesting alternative to silicon-based *p*-layers for a-Si:H. In principle, one can obtain highly variable bandgaps and band alignments relative to a-Si:H. Our hope in these studies has been to demonstrate high open-circuit voltages in heterostructure a-Si:H cells using polymer *p*-layers, which would be of fundamental interest (in establishing V_{OC} device physics), and could conceivably be of technological significance. The use of heterostructure *p*-layers has been quite successful for c-Si HIT cells, and, technically speaking, the present microcrystalline Si and a-SiC:H *p*-layers used for a-Si:H based solar cells are heterostructure devices.

Our experimental work has explored doped polyaniline, cast onto the Si layer, as the hole-conducting polymer. We had hoped this material would be preferable for casting onto Si, since it uses a non-aqueous solvent (typically xylene) and might yield thinner oxide layers near the interface than polymers using water as the solvent. While we are able to fabricate decent diodes this way, the open-circuit voltage remains at least 0.1-0.2 V below values with conventional, inorganic *p*-layers. Furthermore, except for a particular variety of highly conducting polyaniline obtained from Ormecon, Inc., the illuminated diodes have poor photocurrent densities.

We have obtained open-circuit voltages in a-Si:H *n/i/polymer* cells up to 0.73 V using "PEDOT:PSS," which is a commercially available hole-conducting polymer. This value is below that obtained with conventional *p*-layers. Interestingly, an NREL/Arizona collaboration has shown that hot-wire a-Si:H cells deposited onto PEDOT:PSS in the *pin* sequence have achieved V_{OC}'s of 0.88 V, which is comparable to the value obtained for this material with the best conventional inorganic *p*-layers. However, unlike the inorganic *p*-layer, the polymer p-layer did not require an a-SiC:H buffer layer to achieve this performance. We did contribute the device modeling to this work, which was recently published [4]. The

modeling illustrated the role of the conduction band offsets at the *p/i* interface in accounting for the success of both buffer layers and of the polymer *p*-layer.

Returning to the polyaniline diodes, we cannot distinguish between the two possibilities of poor alignment of the polymer's valence band with that of Si, or the formation of an interface region with completely unknown properties. However, it is fairly clear that polyaniline is unlikely to form a good *p*-layer for a-Si:H and c-Si based solar cells, and we plan to evaluate additional polymers in the coming year.

Published work from this task:

"Polyaniline on crystalline silicon heterojunction solar cells," Weining Wang and E. A. Schiff, *Appl. Phys. Lett.* **91**, 133504 (2007).

"Conducting polymer and hydrogenated amorphous silicon hybrid solar cells," E. L. Williams, G. E. Jabbour, Q. Wang, S. E. Shaheen, D. S. Ginley, and E. A. Schiff, *Appl. Phys. Lett.* **87**, 223504 (2005).

Optical Properties of n/i and p/i Interfaces

In an extensive collaboration with BP Solar (G. Ganguly), we explored the optical absorption spectra of interface states at the *n/i* and *p/i* interfaces. The goal was to create a better understanding of the near-interface region. For one sample series, there is a pronounced effect of the doping level for the *n/i* interface, indicating a change in the character of doping near 1%. One possibility is that doping occurs via dopant-dangling bond complexes at higher doping levels.

"Infrared Charge-Modulation Spectroscopy of Defects in Phosphorus Doped Amorphous Silicon," Kai Zhu, E. A. Schiff, and G. Ganguly, in *Amorphous and Heterogeneous Silicon-Based Films- 2002*, edited by J.R. Abelson, J.B. Boyce, J.D. Cohen, H. Matsumura, J. Robertson (Materials Research Society Symposium Proceedings Vol. 715, Pittsburgh, 2002), 301--306.

A. Characterization & Modeling of a-Si:H Solar Cells

1. Introduction

The device physics of *pin* solar cells involves – at a minimum – three different materials as well as the interfaces between them. Since the invention of hydrogenated amorphous silicon (a-Si:H) *pin* solar cells about thirty years ago, an enormous effort by scientists around the world has generated a correspondingly large number of papers detailing the optoelectronic properties of the materials. There have also been a number of pioneering efforts to integrate this information into models for the device physics of the cells [14- 19]. The task of achieving useful insight when models have dozens of relevant parameters is daunting, and it is probably fair to say that there is no consensus understanding about how the cells work.

In this paper we first describe the *hole-mobility limit* of the efficiency for *pin* solar cells with absorber layers. Such a limit, which typically applies when hole drift-mobilities are less than around 1 cm^2/Vs, is implicit in any of the device models for a-Si:H, but has been little explored since seminal work of Crandall [14]. The remarkable aspect of the hole-mobility limit is that it depends quite weakly upon processes that might seem more important, including photocarrier recombination and electron mobilities (which are assumed to be much larger than the hole mobilities).

For intrinsic a-Si:H, we summarize the many measurements of hole drift-mobilities; these mobilities are very low (typically less than 10^{-2} cm^2/Vs), although there have been promising reports of better mobilities. These mobility measurements are sufficient to establish a "hole mobility limit" for single-junction cells with an a-Si:H intrinsic layer, and we show that a-Si:H *nip* solar cells prepared at United Solar Ovonic Corp. have achieved solar conversion efficiencies that are very close to the hole mobility limit. This achievement is a remarkable one. It implies that dangling bond densities have been kept low enough that they do not dominate the drift of holes, and that the *n* and *p* layers are good enough to act as nearly ideal electrodes to the cell.

These conclusions apply to the "as-deposited" state of the cells. In use, a-Si:H based solar cells are light-soaked. Plausibly, the dangling bond density in the cells rises sufficiently to reduce the output power below the hole-mobility limit. The saturated degradation in the power is about 30% for thick single-junction cells that lack optical enhancements such as back reflectors and texturing [26]; the decline is less in optimized cells. The conclusion that the as-deposited cells are near their hole mobility limit then creates a puzzle, for it seems an unlikely coincidence that the light-soaking process should saturate just when cells show noticeable (30% or less) degradation. We therefore speculate that the light-soaking process is "self-limiting" in the cells we have studied, and we discuss an obvious – but insufficient – mechanism for self-limitation in the concluding section.

2. Hole-mobility Limit for *pin* Solar Cells

Perhaps the most elementary model for a *pin* solar cell assumes uniform photogeneration G in the intrinsic layer, and describes transport and recombination in this layer using only hole and electron mobilities μ_p and μ_n and an interband recombination coefficient b_R. For sufficiently low hole mobility $\mu_p << \mu_n$, and ideal *n* and *p* layers, this model yields a fairly simple approximation for the maximum power density from a thick cell [20]:

$$P = \left((2/3)V_{OC}\right)^{3/2}\left(\mu_p \varepsilon (eG)^3\right)^{1/4} \tag{1}$$

where the open-circuit voltage V_{OC} is given by:

$$eV_{OC}^0 = E_G + kT\ln\left(\frac{G}{b_R N_C N_V}\right)\ ; \tag{2}$$

E_G is the bandgap of the material, N_C and N_V are the bandedge densities-of-states, e is the fundamental

charge, k is Boltzmann's constant, and T is the temperature (in Kelvins). ε is the permittivity of the absorber (SI units); we use the value $\varepsilon = 1.05\times10^{-10}$ C^2/N-m^2 that is typical of a-Si:H.

The expression for V_{OC} is independent of the carrier mobilities. This aspect is important, and is fairly readily understood from the perspective that eV_{OC} reflects the splitting of the electron and hole quasi-Fermi levels E_{Fn} and E_{Fp} in the intrinsic layer [20]. By definition, $E_{Fp} = E_V - k_B T \ln(p/N_V)$; a similar relation holds for E_{Fn}. These expressions are not directly related to mobilities. The same perspective accounts for V_{OC}'s logarithmic dependences upon b_R, N_C, and N_V.

The expression for the power density P depends directly only on the ¼ power of the hole mobility μ_p and the ¾ power of the generation rate G. It has a weak dependence upon recombination parameters through V_{OC}.

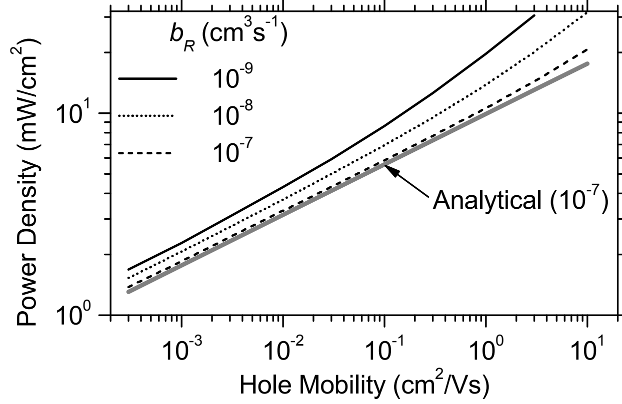

Fig. 1: Calculations of the power density from a thick *pin* solar cell as a function of the hole mobility for uniform photogeneration 3.3x10^{20} cm^{-3}s^{-1}. Numerical calculations for three values of the recombination coefficient b_R are shown as black lines; the gray line is from an analytical expression (eq. (1) of the text) using $b_R = 10^{-7}$ cm^{3}s^{-1}.

These analytical expressions are based on an approximate analysis that neglects the roles of diffusion. It is thus important to confirm them using a full numerical study of the same physical model. The black lines in Fig. 1 illustrate calculations of P done using the AMPS-1D computer code [17] for G = 3.3x10^{20} cm^{-3}s^{-1}, which was selected because it has the same magnitude that solar illumination makes in a-Si:H. Results are shown for three values of the interband recombination coefficient b_R [21]; the value for a-Si:H is around $b_R = 10^{-9}$ cm^{3}s^{-1}. The gray line is the analytical approximation (eq. (1)) for $b_R = 10^{-7}$ cm^{3}s^{-1}. Eq. (1) gives a good approximation to the full computer simulation over this range of hole mobilities. For larger values of μ_h, the power is larger than expected from eq. (1); the increase reflects the increased importance of ambipolar diffusion, which was neglected in deriving eq. (1).

Fig. 2 presents profiles of the "collection efficiency" $1-G/R$ (R is the recombination rate at a particular position x) and of the electric field as they were calculated for the maximum power point using the AMPS 1-D code. The simulations were done for very thick absorber layers (30 μm); photocarrier collection is only significant in the *p*/*i* interface region that is illustrated. The profiles on the left-hand side are calculated for a low hole mobility 0.003 cm^2/Vs. These graphs illustrate that the electric field is confined to a fairly narrow region (width d_C) near the *p*/*i* interface. In addition, the photocarrier collection efficiency is only significant within this "collection width," from which one draws the inference that the field-assisted drift of holes dominates the cell.

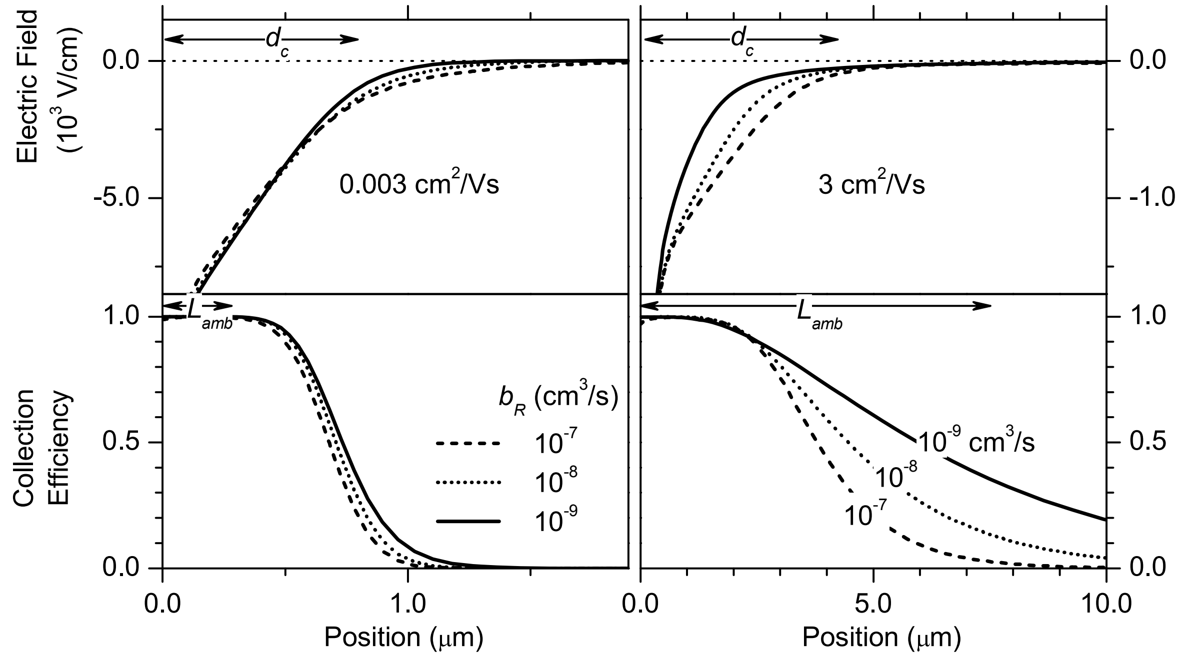

Fig. 2: Calculations of the profiles for the photocarrier collection efficiency $1-G/R$ and the electric field for a simple model of a *pin* solar cell; G= 3.3x10^{20} cm^{-3}s^{-1}. Graphs on the left side of the figure are calculated using a hole mobility of 0.003 cm^2/Vs; the three curves show these profiles for 3 values of the recombination coefficient b_R. Note that a factor 100 change in b_R has little effect on the profiles. The graphs also illustrate the field-assisted collection length d_C and the ambipolar diffusion length L_{amb} for b_R.= 10^{-9} cm^{3}s^{-1}; the small effects of b_R and the inequality $L_{amb} < d_c$ are important characteristics of the low-mobility limit. Graphs on the right side illustrate similar calculations for a cell with a higher hole mobility (3 cm^2/Vs) for which the low-mobility characteristics are less evident.

This conclusion is consistent with the small magnitude of the ambipolar diffusion length $L_{amb} = \sqrt{2(kT/e)\mu_p \tau_R}$ for this mobility; for the present model $\tau_R = (Gb_R)^{-1/2}$. The two profiles on the right side of the figure illustrate the solutions for a much larger hole mobility 3 cm^2/Vs. For the smallest recombination coefficient b_R = 10^{-9} cm^{3}s^{-1}, photocarrier collection is dominated by ambipolar diffusion. The low-mobility behavior is restored for b_R = 10^{-7} cm^{3}s^{-1}, as can also be inferred from Fig. 1.

3. Hole Drift-Mobilities in a-Si:H

Fig. 3 shows the drift-mobility of holes near room-temperature for five a-Si:H samples. ECD94 is a plasma-deposited sample prepared around 1989; its hole drift-mobility is about the same as was reported for other samples prepared in the 1980's [22]. BP03 is a plasma-deposited material prepared fairly recently that used hydrogen-diluted silane as the source gas [23]. Eindhoven05 was prepared using the expanding thermal plasma method [24], and Palaiseau03 is a "polymorphous" sample [25]. It seems apparent that hole drift-mobilities in a-Si:H have increased in the last decade. It is not clear at present how each of the changes in deposition procedures (hydrogen dilution, pressure, reactor design) has contributed to this improvement.

For solar cell applications, the most significant aspect of this graph is that the magnitudes of the drift-mobilities for recent samples range from 6x10^{-3} to 2x10^{-2} cm^2/Vs. Casual inspection of Fig. 1 indicates that the maximum power densities for cells with such mobilities are roughly the same as for a-Si:H single-junction solar cells; simplified cells that do not exploit "optical engineering" (light-trapping and advanced back reflectors) typically have an initial power density of 7 mW/cm^2 under a solar simulator [26]. We show results from a more accurate model for a-Si:H in the next section.

We digress briefly to discuss the construction of Fig. 3. It is not common to present drift-mobilities for different materials and from different laboratories on a single graph. The reason for this is the "dispersive" property of hole drift in a-Si:H and most other low-mobility semiconductors. Measurements of the photocarrier "time-of-flight" t_T yield estimates of a drift-mobility through the expression:

$$\mu_d \equiv d^2 / 2Vt_T ,$$

where d is the sample thickness and V is the bias voltage used in the measurement [27]. Experimentally, these drift-mobility estimates depend significantly upon the voltage that is applied; although rarely performed, the estimates also depend upon thickness. It isn't obvious how to compare different materials except using the cumbersome approach of arranging for samples of identical thickness measured at some particular voltage.

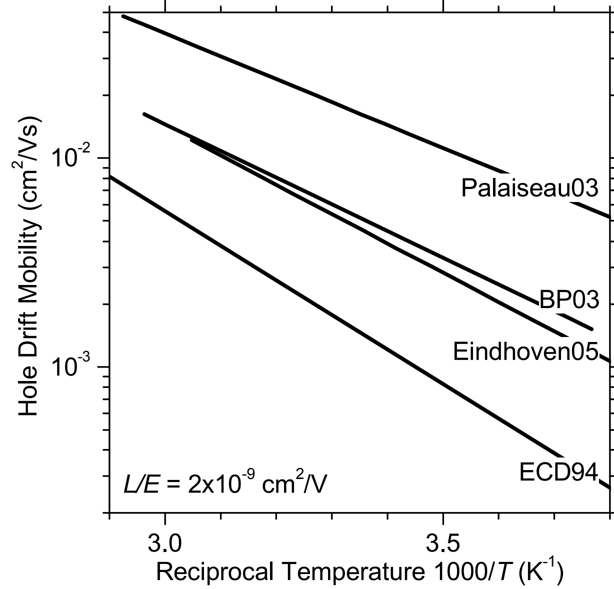

Fig. 3: Hole drift-mobility measurements as a function of temperature for five a-Si:H samples evaluated at a displacement-field ratio $L/E = 2\text{x}10^{-9}$ cm^2/V. Definitions of the sample codes are given in the text.

This voltage-dependence of μ_d does not imply that photocarrier transport is nonlinear with electric field E. The displacement $x(t)$ of a sheet of carriers over a time interval t does (usually) depend linearly upon E. The voltage dependence is instead a consequence of "dispersive transport" [28], which is evidenced in the power-law decays of the photocurrent transients used to measure the transit times. It can be shown fairly generally that the drift-mobility μ_d depends only on the "displacement field ratio" L/E [29]. Different materials can thus be compared – even in the presence of dispersive transport – at common values of L/E, and this was done to prepare Fig. 3 [30]. The lines shown in Fig. 3 are actually best-fits to the temperature-dependent hole drift-mobilities over the range of temperatures illustrated.

4. Amorphous Silicon *nip* Solar Cells: Solar Illumination

In order to account for the strongly temperature-dependent and dispersive character of hole drift-mobilities in a-Si:H, a model incorporating an exponential valence bandtail has long been used [31]. The bandtail states act as traps for holes and as recombination centers; such bandtail states are provided for by the commonly used modeling codes including AMPS-1D [17] and ASA [32]. The simplest version of the valence bandtail model requires two additional parameters beyond those already introduced. These are the width of the bandtail ΔE_V, and the valence bandtail trapping coefficient b_{vp} that describes capture of mobile holes by these traps.

In Fig. 4 we present a numerical calculation (AMPS-1D code) of the dependence of the power density of a-Si:H solar cells upon the thickness of the intrinsic layer for solar illumination. The electronic parameters of the model are presented in Table I; they have been published previously [33]. The hole transport parameters μ_p, ΔE_v, and b_{vp} are consistent with two samples in the middle of the range of Fig. 3. The bandtail recombination parameter $b_{vn} = 10^{-9}$ cm^3s^{-1} has been taken from two independent high-intensity photoconductivity measurements [34,35]. The valence bandtail density at the bandedge $g_v^0 = 6 \times 10^{21}$ $cm^{-3}eV^{-1}$ is not independent in the present model [20,33], but is required for actual calculations. The bandedge parameters N_C and N_V were chosen to be consistent with measurements of the temperature-dependent open-circuit voltage measurements. The bandgap E_G and the optical absorption spectra were consistent with direct optical measurements. Electron mobility parameters are given for completeness, but the calculations are insensitive to the precise values shown.

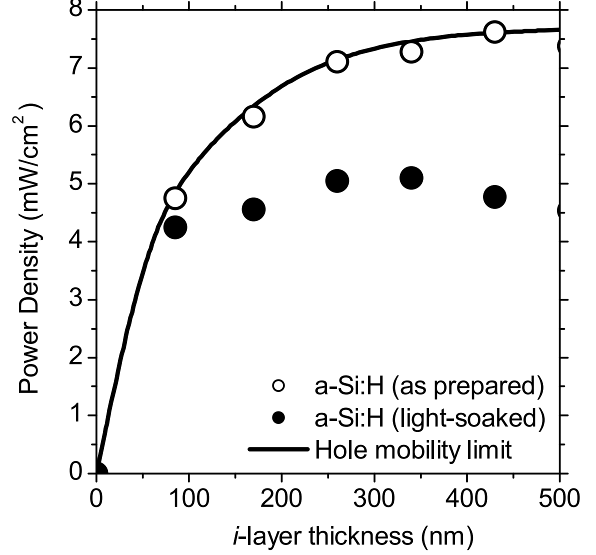

Fig. 4: Power output of a-Si:H *nip* solar cells for varying *i*-layer thicknesses (AM1.5 illumination). The symbols represent measurements on cells made at United Solar Ovonic Corp. [26]. The line is a computer calculation that illustrates the maximum power consistent with hole drift-mobility measurements (see text).

For the present calculations, the apparent "hole mobility limit" is the saturated value of the power found for very thick cells, which is about 7 mW/cm^2 for the present calculation. As it does for the simpler model of section 2, the value of the recombination parameter b_{vn} does have a slight effect on the calculation; decreasing b_{vn} by a factor 10 increases the saturated power by 6%. This percentage, calculated for white light illumination, is a bit misleading, since strongly absorbed green and blue photons are collected very readily. For red illumination, and more homogeneous absorption, reducing b_{vn} tenfold increases the power for thick cells by 13%. Increasing the hole band mobility μ_p tenfold increases the power for red illumination by 95%. These values are reasonably consistent with the results for the simpler model of Fig. 1 and a typical mobility parameter $\mu_p = 10^{-2}$ cm^2/Vs (cf. Fig. 3 at T= 295 K).

Device-makers are sometimes surprised by the prediction of a saturated power for larger thicknesses in these models, since working cells can show a decline in power for larger thicknesses. While this issue has not been

Table I: a-Si:H Solar Cell Modeling Parameters [33]. Solar cell performance is mainly sensitive to the boldfaced parameters.

$\boldsymbol{\mu_p}$	0.3 cm^2/Vs	Band-mobility of holes.
$\boldsymbol{\Delta E_v}$	0.04 eV	Width of exponential valence bandtail.
$\boldsymbol{N_v}$	4×10^{20} cm^{-3}	Valence band effective density-of-states.
$\boldsymbol{b_{vp}}$	1.3×10^{-9} cm^3s^{-1}	Trapping coefficient $h^+ \rightarrow V^0$ (valence bandtail).
$\boldsymbol{E_g}$	1.74 eV	Electrical bandgap.
b_{vn}	1.0×10^{-9} cm^3s^{-1}	Trapping coefficient $e^- \rightarrow V^+$ (valence bandtail).
μ_n	2 cm^2/Vs	Band-mobility of electrons.
ΔE_c	0.02 eV	Width of exponential conduction bandtail
N_c	4×10^{20} cm^{-3}	Conduction band effective density-of-states.
b_{cn}	1.3×10^{-9} cm^3s^{-1}	Trapping coefficient $e^- \rightarrow C^0$ (conduction bandtail)

definitively studied, calculations with highly reflecting back contacts do show a peak power for some optimum thickness, and a decline for thicker cells [36].

The experimental measurements of Fig. 4 are for a series of a-Si:H single-junction *nip* solar cells prepared at United Solar Ovonic Corp. [26]. The cells are deposited directly onto stainless steel substrates, which have a fairly low reflectivity. Production cells that are deposited onto textured, highly reflecting back contacts have larger power output. On the other hand, these simpler cells are fairly well suited to comparison with model calculations, and as can be seen in the figure, the "as-deposited" cells agree reasonably well with the calculation. The light-soaked cells were exposed under open-circuit conditions for the unusually long time of 30,000 hours, and of course have lower power output than the as-deposited cells.

5. Amorphous Silicon Solar Cells: Uniformly Absorbed Illumination

In this section, we present temperature-dependent measurements and analyses for a series of a-Si:H *nip* solar cells prepared at United Solar Ovonic Corporation that indicate that the efficiencies of these cells at solar intensities are mostly determined by the hole mobility of the intrinsic layer. Essentially the same conclusion (of mobility or space-charge limited photocurrent) was reached recently for polymer-fullerene blend solar cells [37] Temperature-dependent measurements are useful for exploring hole mobility effects in a-Si:H solar cells because the strong temperature-dependence of the hole drift-mobility in a-Si:H gives a fairly distinctive temperature-dependence for the cell efficiency. The statement that the efficiencies are near the hole mobility limit implies that the density of deep levels is sufficiently low that it has a minor effect on the efficiency, and that the *p/i* and *n/i* interfaces are sufficiently good that they are behaving nearly ideally. We also present measurements for the light-soaked state, where deep levels do have a clearly measurable effect; the mobility-limitation idea remains roughly applicable. We conclude that improved efficiencies of a-Si:H solar cells will likely require further improvements in the hole drift-mobility.

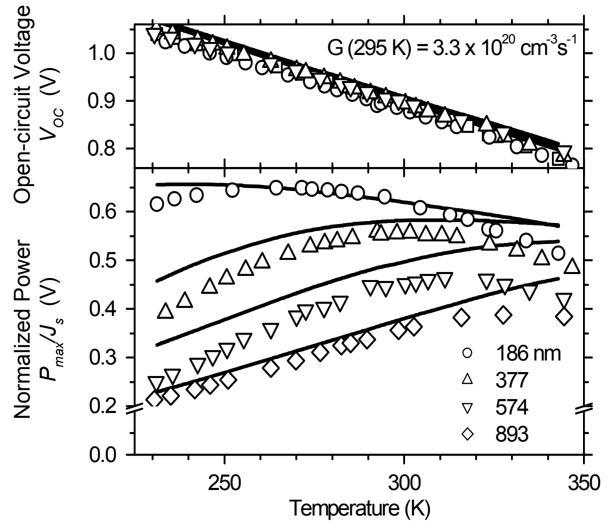

Fig. 5. Temperature-dependent measurements of V_{OC} and the P_{MAX}/J_s for four as-deposited a-Si:H *nip* solar cells with varying intrinsic layer thickness are indicated by the symbols. Measurements were done at constant laser flux; the average photogeneration rate G at 295 K was 3.3×10^{20} cm^{-3}s^{-1}. The lines indicate corresponding calculations for a model based primarily on hole drift-mobility measurements.

For these experiments, six a-Si:H *nip* solar cells were deposited at United Solar Ovonic Corp. using RF glow discharge on stainless steel substrates. The *n* and *p* layers were the same in all depositions; the deposition time for the intrinsic layer was chosen to give intrinsic layer thicknesses from 185 nm to 893 nm. The cells were not optimized for the best efficiency, and in particular do not have a highly reflecting back contact. Special attention was paid to the hydrogen dilution in the intrinsic layer to maintain a good material quality throughout the entire intrinsic layer and to avoid nanocrystallite inclusion. Details of the deposition procedures have been given elsewhere [38]. As-deposited properties of the cells were measured under a solar simulator; for the thickest intrinsic layer (893 nm) a typical cell had an open-circuit voltage (V_{OC}) of 0.982 V, a short circuit current density (J_{SC}) of 14.4 mA/cm^2, a fill factor (FF) of 0.559, and a maximum power density (P_{MAX}) of 7.9 mW/cm^2.

Further studies were done using a 30 mW, near-infrared (685 nm wavelength) laser. We chose to use this laser because its wavelength is absorbed fairly uniformly throughout the intrinsic layers of the cells, which simplifies modeling of the measurements. In Fig. 5 we present the temperature-dependent normalized maximum power density $P_{MAX}(T)/J_s(T)$ and $V_{OC}(T)$ for four cells with differing intrinsic-layer thickness. J_s is the photocurrent density measured at –2 V, which is a good approximation to the saturated reverse-bias photocurrent over most of the temperature-range. The measurements were done at constant laser flux. The average photogeneration rate at 295 K was $G = 3.3\times10^{20}$ cm^{-3}s^{-1}; G does vary with T due to the temperature-dependent bandgap of a-Si:H.

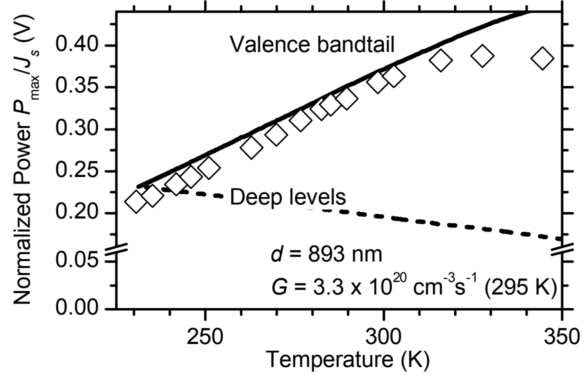

Fig. 6. Temperature-dependent calculations for P_{MAX}/J_s of an a-Si:H *nip* solar cell based on a deep-level model are shown as the dashed line; the intrinsic layer thickness is 893 nm. The corresponding experimental measurements (symbols) and valence bandtail based calculations from Fig. 1 are also shown for reference.

As has been reported by most previous workers, V_{OC} is nearly thickness-independent. P_{MAX}/J_s declines markedly with thickness, which indicates that photocarriers generated deep inside a thick cell are likely to recombine instead of contributing to power generation. The solid lines in Fig. 5 represent computer calculations (AMPS-1D code17) using what we consider to be the simplest reasonable model for an a-Si:H *nip* solar cell. The crucial electrical parameters describe hole transport in the intrinsic layer. The code uses the exponential valence bandtail trapping model [39,40] to describe hole transport. The parameters we used are given in Table I; as described elsewhere [41], they have been chosen for consistency with hole drift-mobility ("time-of-flight") measurements [42]. The electron parameters are given in Table I for completeness, but the calculations are fairly insensitive to them. This is expected because electron drift-mobilities are hundreds of times larger than hole drift-mobilities in a-Si:H [40,20] Deep levels were not included in the calculations of Fig. 5. We used idealized *p* and *n* layer parameters for which the precise values have little effect on calculated cell properties; prior experiments indicate that doped layers and interfaces are not limiting V_{OC} in contemporary cells [43] The temperature-dependent photogeneration rate $G(T)$ was determined from the measured, temperature-dependent photocurrent under reverse bias for the thinnest cell (186 nm). The temperature-dependent bandgap $E_G(T)$ was determined from measurements of the electroabsorption spectrum that are not shown here; this method [44] gave results consistent with earlier reports [45].

As can be seen from the figure, these calculations give a good account for the temperature-dependent magnitudes of V_{OC} and P_{MAX}/J_s. The near thickness-independence of V_{OC} and its increase with decreasing temperature may be roughly understood using the model that equates eV_{OC} (e is the electronic charge) to the separation of electron and hole quasi-Fermi levels in the intrinsic layer [39,40] For the thicker samples, the decline in P_{MAX}/J_s with decreasing temperature is a consequence of the rapid decline in the hole drift-mobility with temperature in a-Si:H [40]. As the hole drift-mobility declines, the region from which holes can be collected shrinks, and leads to reduced power from a thick cell [20] At the highest temperatures, there is evidently a discrepancy between the model and the P_{MAX}/J_s measurements; we believe that this reflects the onset of the effects of deep levels (dangling bonds).

Modelers generally include deep levels when they study a-Si:H solar cells[17,19] but we do not believe that deep levels dominate the values of P_{MAX} and V_{OC} of the as-deposited cells studied here. One reason for our view is that the measured drift mobilities of holes in a-Si:H essentially establish the largest values of P_{MAX} that can be obtained from the cells, and Fig. 1 indicates that the actual power from cells is close to

these maximum values. If the densities of deep levels were large enough, they would lower P_{MAX} and V_{OC} noticeably below the calculated values of Fig. 5. A second reason for believing that a density of deep levels is not dominating V_{OC} and P_{MAX} is illustrated in Fig. 6, where the dashed line is a calculation of P_{MAX}/J_s based on the assumption that deep levels do dominate hole trapping. P_{MAX}/J_s calculated using deep levels decreases as the temperature T increases; both the measured P_{MAX}/J_s and the calculation based on hole mobilities increase with T.

For the deep level calculation in Fig. 6, we set the bandtail trap densities to zero. We used a donor-type (0/+) deep level that was electrically neutral in the dark. The coefficients for hole and electron capture by the deep level chosen to be $b_{dp} = 7.5\times10^{-9}$ and $b_{dn}= 4\times10^{-8}$ cm^{3}s^{-1}, respectively. Given $\mu_p = 0.3$ cm^2/Vs, they are consistent with hole deep-trapping experiments [46]. We neglected the slight temperature-dependences. The defect density N_d is 5.7×10^{16} cm^{-3} for Fig. 2, which fits the measured power at 230 K.

While deep levels do not seem to have a noticeable effect on the as-deposited state of these cells, a growth in deep-level density during illumination is the most plausible mechanism for the degradation of a-Si:H based solar cells during light-soaking [47]. In Fig. 7 we present the measurements for V_{OC} and P_{MAX}/J_s for an 893 nm cell before and after 200 hours of light soaking at 295 K ($G = 3.3\times10^{20}$ cm^{-3}s^{-1}). The P_{MAX} measured at 295 K degraded about 30%, which is comparable to the saturated degradation of thick cells after long-term exposure to solar illumination.[26] It is interesting that there is little difference in the light-soaked and the as-deposited states when measured at 230 K. This convergence of the two states at lower temperatures has not, to our knowledge, been noted in previous solar cell studies.

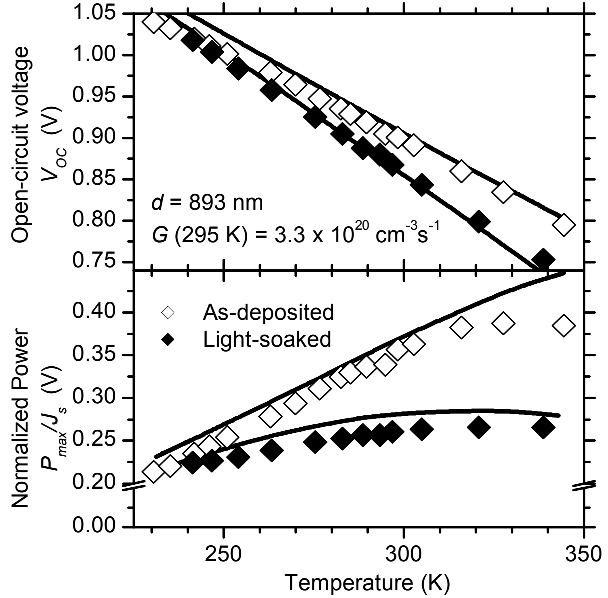

Fig. 7. Symbols indicate temperature-dependent measurements of V_{OC} and P_{MAX}/J_s for an 893-nm thick cell in its as-deposited and light-soaked (200 hours at 295 K) states. The calculated line through the as-deposited measurements is from the hole drift-mobility based calculation of Fig. 5; for the light-soaked state, the calculation also includes a density of deep levels.

We were able to account for the convergence effect using the modeling procedures described above. For the light-soaked state, we added a density of deep levels to the bandtail traps that were used to calculate the properties of the as-deposited state [48]. The deep level trapping coefficients b_{dp} and b_{dn} were noted earlier; the density of defects N_D was adjusted to 2×10^{16} cm^{-3} in order to fit the measured value of V_{OC} at 295 K after light-soaking. This calculation gives a satisfactory account for the magnitude of P_{MAX}/J_s (no parameters were further adjusted), as well as for the temperature-dependences of V_{OC} and of P_{MAX}/J_s. The measurements of V_{OC} at lower temperatures are somewhat smaller than the calculated values. We speculate that this effect is due to a non-ideal p-layer.

Heuristically, the convergence effect may be understood from the splitting of the electron and hole quasi-Fermi levels in the intrinsic layer. This splitting increases as T falls (as evidenced by $V_{OC}(T)$). While the density of deep levels is constant, the density of bandtail states between the two quasi-Fermi levels increases with this splitting – thus accounting qualitatively for the increased importance of bandtails at lower T.

6. Light-Soaking Kinetics of the Open-Circuit Voltage

Introduction

The metastable degradation of the optoelectronic properties of a-Si:H has been actively studied for more than 25 years. Important progress has been made by many researchers, but a fully satisfactory picture for the effect has never emerged. The difficulty of the metastability problem may, at least in part, be ascribed to the fact that there are probably two difficult, linked problems that must be understood simultaneously. First, it is likely that photocarrier recombination drives metastability, but - even for a single light-soaking state of an a-Si:H sample - no consensus viewpoint on these recombination processes has emerged. Second, even if one accepts the role of recombination in mediating metastability, there is no consensus viewpoint about how recombination leads to degradation by defect generation or other metastabilities.

The present section exploits the close connection between the open-circuit voltage V_{OC} measured in an *nip* solar cell and photocarrier recombination in the bulk, intrinsic-layer material. In particular we report a series of measurements of the time-dependent degradation of V_{OC} in United Solar cells under near-solar illumination. In recent work [49] we reported the temperature-dependence of V_{OC} at solar illumination intensities. We concluded from these studies that, for their as-deposited state, the recombination traffic in our samples flowed predominantly through the valence bandtail states. For the stabilized, light-soaked state recombination traffic appears to be split fairly evenly between the valence bandtail and defects. We emphasize that these conclusions apply to our materials, under near-solar illumination, and near room-temperature; these are, of course, the conditions of greatest practical significance for solar cells.

Using this recombination model as the starting point, we have been able to account for the time-dependent decay of V_{OC} using a straightforward extension of the hydrogen-collision model [50] for defect generation; the extension assumes that mobile hydrogen is generated by bandtail recombination. For our materials, we can also exclude the best known alternative model [51].

There is at least one implication of this perspective on metastability that deserves further investigation. It appears that there is a coincidence of two time-scales: (i) the time at which crossover between bandtail and defect recombination occurs, and (ii) the time at which a stabilized state of the sample is achieved. The coincidence suggests that defect recombination may mediate light-induced annealing.

Measurements

As-deposited properties of the cells were measured under a solar simulator. This paper emphasizes results for the thickest cells, for which the white-light V_{OC} averaged 0.98 V and the white-light fill factors averaged 0.66.

The present measurements were done using a 30 mW, 685 nm wavelength near-infrared laser. We chose to use this laser because its wavelength is absorbed fairly uniformly throughout the intrinsic layer of the cells, which substantially simplifies modeling of the measurements. We were able to achieve photocurrent densities in the cells that were comparable to solar illumination.

Measurements of the decline of the open-circuit voltage V_{OC} are presented in Fig. 8. The different symbols indicate measurements for four different laser intensities. We used four different cells on the same substrate for these measurements; the cells had very similar initial properties under white-light. The average photogeneration rates G for each experiment are indicated in the figure; these were calculated from the measured photocurrent density J_p at V_r = -2 V using the expression $G = J_p(-V_r)/ed$, where e is the electronic charge and d is the thickness of the intrinsic layer. The measurements for the highest intensity are most comparable to solar illumination (saturated photocurrent density was 18 mA/cm^2 with the laser, and about 15 mA/cm^2 with the solar simulator). We monitored the sample temperature during these measurements, which was maintained at 294.5 K to within better than 0.1 K.

An interesting feature of the measurements is that the onset of degradation occurs for later times at lower photogeneration rates. If we define an "onset time" when V_{OC} has declined by 0.01 V, it is evident in Fig. 1 that this onset time increases by more than 1000 over the range of photogeneration rates in the figure. For the largest photogeneration rate it appears that V_{OC} is approaching a saturation value within this time window; saturation at longer times is fairly well-established in earlier work on solar cell parameters, defect density, and other optoelectronic properties of a-Si:H.

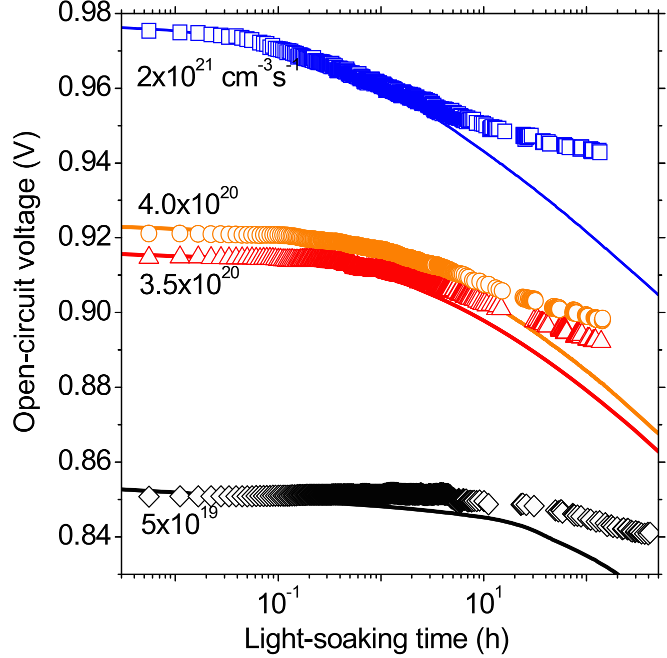

Fig. 8: Decay of the open-circuit voltage with time at four different intensities; the average photogeneration rate in the intrinsic layer is indicated. The symbols denote the experimental measurements in four cells (893 nm *i*-layer thickness, laser wavelength 685 nm) on the same substrate. The lines represent calculations for the "extended hydrogen-collision model" described in the text.

A Modified H-Collision Model

We presented temperature-dependent measurements on the open-circuit voltage for a-Si:H cells from the same substrate used for Fig. 8. These measurements for the as-deposited and the light-soaked states are consistent with the following model. For the as-deposited states of a-Si:H, the photocarrier recombination traffic is predominantly through the valence bandtail (through the process of electron capture by a bandtail-trapped hole). Light-soaking then has a surprisingly modest effect: the defect-density rises until recombination traffic is fairly evenly split between the bandtails and the defects.

One important fact that has been established in several light-soaking experiments [51- 54] is that the defect density increases as about the 1/3 power of the light-soaking time: $N_d \propto t^{1/3}$ essentially from the onset of illumination until a saturated state is achieved. The original "SJT" explanation [51] for the $t^{1/3}$ form made two assumptions. First, recombination traffic through the bandtails R_t generated defects:

$$\frac{dN_d}{dt} \propto R_t \quad . \qquad (1)$$

Second, for times at which the $t^{1/3}$ form applied, most recombination traffic went through defects $R_d \approx G$. The particular model that was proposed had the property that the fraction of the recombination traffic through the tails obeyed:

$$R_t / G \propto 1/N_d^2 \,, \qquad \text{(SJT recombination) (2)}$$

where G is the carrier photogeneration rate and N_d is the density of defects. With this assumption, one obtains the form usually found by experiment:

$$N_d(t,G) = 3C_{SW}G^{2/3}t^{1/3} \quad . \qquad (3)$$

At least for the samples we have studied, SJT-recombination does not apply over a significant time-regime. Recombination traffic mostly passes through the bandtail states ($R_t \approx G$) in the as-deposited state, and falls only modestly even for the saturated, light soaked state. Although we have not studied the growth of the defect density during light-soaking with these particular samples, the near-universality of the observation of the $t^{1/3}$ form for $N_d(t)$ suggests that we seek an alternative to SJT-recombination for the kinetics of light-soaking. A similar situation also applies to light-soaking with intense pulses. Bandtail recombination is completely dominant, but defect growth shows a sublinear dependence on illumination time [55].

The principal alternative to the SJT approach is the "hydrogen-collision" model [50], which assumes the existence of an illumination-induced mobile hydrogen density H_m obeying:

$$H_m \propto G_H / N_d \,. \qquad (4)$$

G_H is the rate at which light generates mobile hydrogen, and it has been assumed that the recombination traffic of hydrogen mostly flows through dangling bonds (density N_d). Rarely, mobile hydrogens "collide" to form a stable, paired hydrogen complex. Such a collision leaves 2 metastable dangling bond that are not present in the initial state; the defect generation rate obeys the "hydrogen-collision" proportionality:

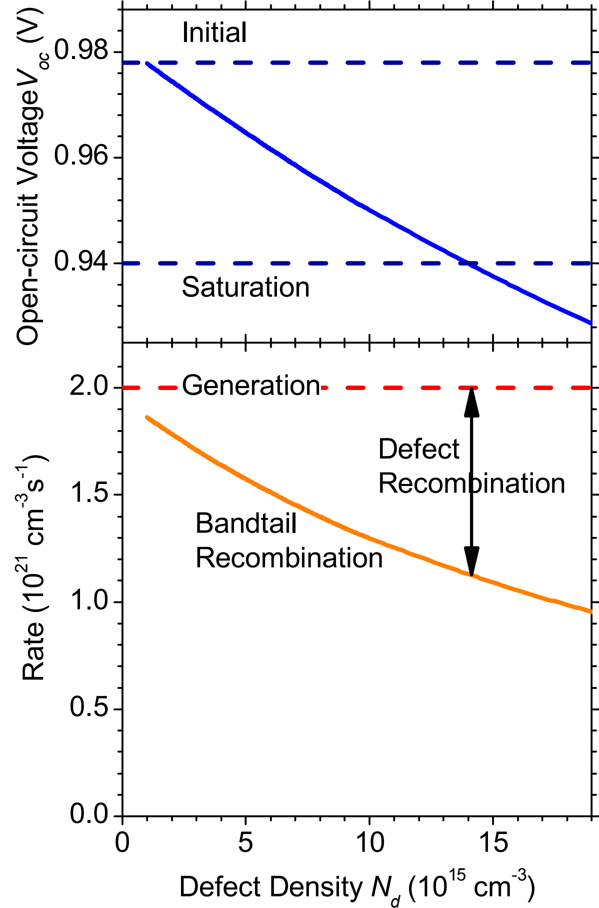

Fig. 9: Bandtail recombination rate R_t and open-circuit voltage V_{OC} calculated as a function of defect density N_d using the bandtail+defect code. The photogeneration rate and defect recombination rate are also shown. The initial experimental value of V_{OC} corresponds to N_d = $1\text{x}10^{15}$ cm^{-3}, and we have suggested a saturation value. Note that bandtail recombination is comparable to G throughout this range of defect densities.

$$\frac{dN_d}{dt} \propto H_m^2 \propto (G_H / N_d)^2 \text{(hydrogen-collision).} \qquad (5)$$

Note that the empirical "$G^{2/3}t^{1/3}$" form for $N_d(t)$ (eq. 3) obtains if we assume that $G_H \propto G$.

The assumption $G_H \propto G$ is arguable; several experiments [56] suggest that defect generation is mediated by photocarrier recombination, and not by direct optical processes as is suggested by this assumption. Given our conclusion for our samples that R_t/G is of order unity through most of the light-soaking process in our samples, we have chosen to explore the modified form for the hydrogen-collision model:

$$\frac{dN_d}{dt} \propto H_m^2 \propto \left(\frac{G_H}{N_d}\right)^2 \propto \left(\frac{R_t}{N_d}\right)^2 ,$$

or, collecting several proportionality constants together as C_{SW}:

$$\frac{dN_d}{dt} = C_{SW}\left(\frac{R_t(N_d)}{N_d}\right)^2 \qquad \text{(modified H-collision) (6)}$$

We have indicated that R_t depends upon the defect density; of course, for $R_t = G$ the usual behavior of equation (3) obtains.

Bandtail+Defect Calculations

In another section of this report, as well as a conference paper [49], we present the parameters and procedures of a "bandtail+defect" calculation of the open-circuit voltage; the calculation used the AMPS-1D computer program (©Pennsylvania State University). In Fig. 8 we have presented (as the four lines) the corresponding calculations for $V_{OC}(t)$ based on eq. (6). Assuming a spatially uniform defect density N_d, we used the bandtail+defect calculation to obtain the dependences of the bandtail recombination rate R_t and of the open-circuit voltage V_{OC} upon the defect density N_d. These results are illustrated in Fig. 8. We then used the function $R_t(N_d)$ to numerically integrate eq. (6) to obtain $N_d(t)$; we used the value $C_{SW} = 10^1$ cm^{-3}s that is typical of direct studies of the defect generation during light-soaking [52,53]. Once $N_d(t)$ has been computed, $V_{OC}(t)$ is obtained from Fig.9

Experimentally, V_{OC} only declines about 0.04 V (to the value denoted "measured saturation"). As may be inferred from Fig. 9, a decline by 0.04 V implies that most of the photocarrier recombination traffic still flows through the bandtails.

For the four intensities, the agreement between the experimental measurements and the calculations is fairly good through the initial stages of the decay of V_{OC}. For longer times the measured values for V_{OC} fall much more slowly than predicted by eq. (6), which undoubtedly corresponds to the onset of the "light-induced" annealing effects reported previously for defect-density measurements [57].

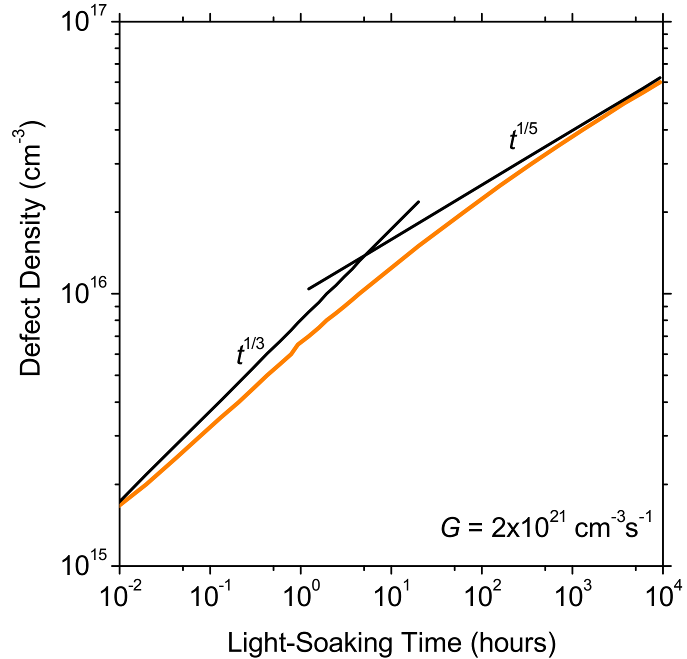

Fig. 10: Calculated growth of the defect density during light-soaking (photogeneration rate 2x10^{21} cm^{-3}s^{-1}); the calculation was based on the hydrogen-collision model of defect generation (C_{SW} = 10 cm^{-3}s) and the bandtail+defect recombination model. The calculation shows a cross-over from $t^{1/3}$ to $t^{1/5}$ kinetics when recombination traffic switches from the bandtails to the defects.

For our experiments, we used laser illumination that was nearly uniformly absorbed; this choice was part of an effort to simplify modeling and to avoid a non-uniform density of defects. Nonetheless, our assumption of a spatially uniform value for N_d as it grew under light-soaking was not self-consistent with the spatial profiles of R_t that were calculated. For the larger values of the density N_d, the bandtail recombination traffic was reduced in a zone about 100-200 nm from the *p/i* interface compared to values in the middle of the cell. We used R_t values from the middle to do the numerical

integration of eq. (6). For full self-consistency we would have needed to allow for a profile of N_d. The profile would have a reduced density of defects as the *p/i* interface was approached from the middle. A rough analysis indicates that inclusion of this effect would improve the agreement between the calculations and the measurements slightly, but we have not pursued non-uniform distributions for N_d further.

Discussion

As noted earlier, the modified H-collision model, in conjunction with the bandtail+defect recombination model, predicts some deviations from the $t^{1/3}$ form for the dependence of the defect density upon the light-soaking time. We did not do simultaneous measurements of the defect density during light-soaking of the present solar cells. In Fig. 10 we show the predictions of the defect density from numerical integration of eq. (6) that corresponds to the highest photogeneration rate we used for experiments.

The calculations show the expected $t^{1/3}$ form for the earlier times. There is a softening that occurs around 10 hours, which corresponds well to a change in the recombination mechanism. For lower defect density, the majority of the recombination traffic goes through the bandtail; for larger densities, the majority goes through defects. A $t^{1/5}$ form is a good fit at longer times. Experimentally, after about 10 hours V_{OC} begins to show saturation behavior (cf. Fig. 8), which we attribute to some "light-induced annealing" process. At least for the present samples, it appears that the long-time saturation effect would obscure direct observation of the $t^{1/5}$ regime.

It is an interesting coincidence that the crossover time between the two recombination regimes and the time at which light-induced annealing sets in are so similar in the present sample. This apparent coincidence is the reason offered by the present viewpoint for the fact that open-circuit voltages decline only modestly during light soaking (roughly by the thermal voltage k_BT/e = 0.025 V), as well as for the fact that most direct experiments on the kinetics of the defect density are reasonably consistent with the $t^{1/3}$ form.

It is unlikely that two entirely independent processes would appear on the same timescale. We therefore speculate that the mechanism underlying light-induced annealing is photocarrier recombination through defects.

B. Hole Drift Mobility Measurements in $CuIn_{1-x}Ga_xSe_2$ Solar Cells

1. Introduction

Over the past decade, polycrystalline $CuIn_{1-x}Ga_xSe_2$ (CIGS) solar cells have achieved impressive efficiencies above 19.5% [58,59]. Efforts to achieve greater insight into this efficiency by understanding the device physics are to some degree confounded by the absence of some of the foundation measurements that are required [60]. In this research, we applied the photocarrier time-of-flight (TOF) technique to determine the drift mobilities of hole photocarriers. Our measurements are apparently the first serious effort to do this. Our findings in brief:

1. Hole drift mobilities are below 1 cm^2/Vs for specimens from both the National Renewable Energy Laboratory and the Institute for Energy Conversion (University of Delaware).
2. The temperature-dependence is weak; the drift-mobility changed about threefold as the temperature fell from 295 K to 100 K in some cells, but this was the largest change. These measurements largely exclude shallow traps as the mechanism for the low drift-mobility, which thus appears to be a property of hole motion at the bandedge itself.
3. Despite the fact that cells from NREL and from IEC both have excellent solar conversion properties, there are significant differences in their measured hole mobilities which need to be considered in modeling work.

There have been prior measurements of hole mobilities using other techniques [61- 64] and the small magnitude of our TOF measurements is somewhat surprising in the context of these earlier measurements. We address these differences in the “Discussion” subsection below.

We have organized this report as follows. We present our measurements for one particular sample from IEC in detail to illustrate our procedures. We then present a summary of the temperature-dependent mobility and the mobility-lifetime products for all our measurements. Finally, we compare our results with related work using Hall effect and admittance measurements to determine mobilities; we speculate that the difference between the admittance and the TOF measurements (which are about ten times smaller) is due to a gradient in the carrier mobility between the bottom and the top of the CIGS films.

2. Specimens

The CIGS thin-film solar cells used for the present measurements were provided by the National Renewable Energy Laboratory (NREL) and by the Institute of Energy of Conservation (IEC) at the University of Delaware. The cells from NREL have the following description [65]. The substrate used is Mo-coated soda-lime glass. The CIGS growth process is NREL's 3-stage process, which incorporates a slight modification in the Ga content and substrate heating profile. Essentially, the Ga content in the first stage (~30% relative to In) is higher than that of the third stage (~25% relative to In). Device fabrication follows by growth of the CdS buffer layer via chemical-bath deposition (CBD) and the ZnO window bilayer grown by RF sputtering. The ~50 nm-thick insulating ZnO is grown from an intrinsic ZnO target, whereas the ~350 nm-thick conductive layer comes from an Al_2O_3-doped ZnO target (2wt%). Cd-free devices skip the CdS deposition step and only use the bilayer ZnO, which is directly deposited on the CIGS absorber. These Cd-free devices use neither `wet' chemistry nor buffer layers to form the junction. The devices are finished with ITO-indium tin oxides electrodes evaporated for the transport properties. The specimen’s areas are shown in Table II, and have been estimated using a magnifying loupe with a built in ruler. All samples incorporate a 100 nm antireflection MgF_2 coating.

The cells from IEC have the following configuration: glass/Mo/$CuIn_{1-x}Ga_xSe_2$/CdS/ZnO/ITO/(Ni/Al grid). The CIGS thin films where grown using elemental thermal evaporation [66] (four source elemental evaporation) on top of a 0.7µm thick sputtered Mo layer. The CdS was deposited by chemical bath (CDB) and has a nominal thickness of 40nm. The last two layers ZnO and ITO were both deposited using RF sputtering, and have thicknesses of 50 nm for ZnO and 0.2 µm for ITO. Finally, the Ni/Al grids were

deposited by electron beam evaporation. The specimen areas were determined by mechanical scribing in order to define an active region. The structural composition and photovoltaic parameters of the specimens used in this research are given in Table II. The photovoltaic parameters of the cells are measured under standard conditions: 100 mW/cm^2, 25° C, ASTM E 892 Global. The structural composition and photovoltaic parameters of the specimen under study are given in Table II.

3. Time-of-Flight Instrumentation

The time-of-fight (TOF) measurements were done using a 3 ns pulsed nitrogen laser-pumped dye laser. The photocurrents were recorded and averaged (for about 100 laser shots to improve the signal-to-noise ratio) using a 500MHz LeCroy digital oscilloscope. The oscilloscope was interfaced to a computer for storage and analysis of the transient waveform.

The specimen was illuminated trough the top layer-n. The laser wavelength was 700nm; the selected wavelength corresponds to a photon energy that exceeds the band gap of CIGS material, E_g = 1.12 eV. and the absorption coefficient [67], α=10^{5}cm^{-1} of the material was large enough to ensure that the photons are absorbed fairly close to top for witch the absorption length is 0.13 µm (within 10% of the active thickness of the specimen), then the transient photocurrent corresponds to holes moving from the top to bottom.

The photocharge generated by the laser was kept well below the CV-charge measured by integrating the displacement current waveform. The repetition rate of the laser was reduced until the transient photocurrent was independent of the repetition rate; a 1 Hz rate was acceptable. We applied forward and reverse biases across the diodes, 1µs prior to the laser pulse; the duration of the pulse was around 30 µs. The *RC* response time of the measuring circuit was comparable in some regimes to the transit time, where the resistance R = 100 Ω (for the amplifier and pulser) and C is the sample's capacitance. We used fairly small sample areas to minimize C.

Table II. Summary of the structural compositions and the photovoltaic parameters of the specimens of $CuIn_{1-x}Cu_xSe_2$. The symbols definition are as follow: E_g is the band gap, V_{OC} is the open circuit voltage, *Jsc* is the short circuit current, *FF* is the field factor, d is the physical thickness of the CIGS absorber layer, and A is the cell area (the area for the IEC devices was obtained by mechanical scribing).

<table>
<tr><td>Sample</td><td>IEC-1</td><td colspan="2">IEC-2</td><td>NREL-1</td><td>NREL-2</td></tr>
<tr><td>Cu/[In+Ga]</td><td>0.82</td><td colspan="2">0.82</td><td>~0.88</td><td>~0.88</td></tr>
<tr><td>Ga/[In+Ga]=x</td><td>0.30</td><td colspan="2">0.30</td><td>~0.30</td><td>~0.30</td></tr>
<tr><td>E_g (eV)</td><td>1.18</td><td colspan="2">1.18</td><td>~1.15</td><td>~1.15</td></tr>
<tr><td>V_{OC} (V)</td><td>0.616</td><td colspan="2">0.636</td><td>0.626</td><td>0.690</td></tr>
<tr><td>J_{SC} (mA/cm^2)</td><td>33.4</td><td colspan="2">32.2</td><td>30.9</td><td>31.2</td></tr>
<tr><td>FF</td><td>72.9</td><td colspan="2">76.1</td><td>68.9</td><td>77.2</td></tr>
<tr><td>Efficiency (%)</td><td>15</td><td colspan="2">15.6</td><td>13.3</td><td>16.6</td></tr>
<tr><td>d (µm)</td><td>2</td><td colspan="2">2</td><td>2.6</td><td>~2 .5</td></tr>
<tr><td>A(cm^2)</td><td>0.0072</td><td>0.0081</td><td>0.008</td><td>0.0132</td><td>0.0132</td></tr>
</table>

4. Capacitance Measurements

The second measurement performed on these samples was capacitance, which is important to assess the field profile inside the sample. We measured the charge transient following a voltage step. The measurements of the charge 3 microseconds after the pulse are illustrated in Fig. 11 for varying pulse heights. As can be seen, there is a moderate nonlinearity of the charge-voltage relation, which corresponds to a voltage-dependent capacitance $C = dQ/dV$ that is also illustrated. Such nonlinearity is usually ascribed to depletion of defects and dopants by the applied bias voltage, and it is a complication for time-of-flight experiments, which are easiest to interpret for strictly uniform fields and negligible depletion.

We use the capacitance to infer an effective, voltage-dependent thickness for our time-of-flight experiments, as we discuss in more detail subsequently. For Fig. 11, at -1.5 V the capacitance corresponds to an effective thickness of 1.8 μm, which is fairly close the physical thickness of the CIGS layer (about 2 μm).

The charge transient measurements also yield an electronic rise-time for our measurements, which convolves ordinary RC effects (from 50 Ohm electronics) and dielectric relaxation effects within the structure. The effects of these times on the transit-time measurements were small, but not completely negligible.

5. Transient Photocharge Measurements

In this section we present the transient photocharge measurements from which we obtained the transit time and the hole drift mobility estimates. The time of flight measures the transit time t_T required to move the mean position of the photocharge distribution a distance L under the influence of the electric field E. Usually, the charge distribution is created at some time t and positioned by an excitation impulse-in the present case, the excitation impulse was a 3

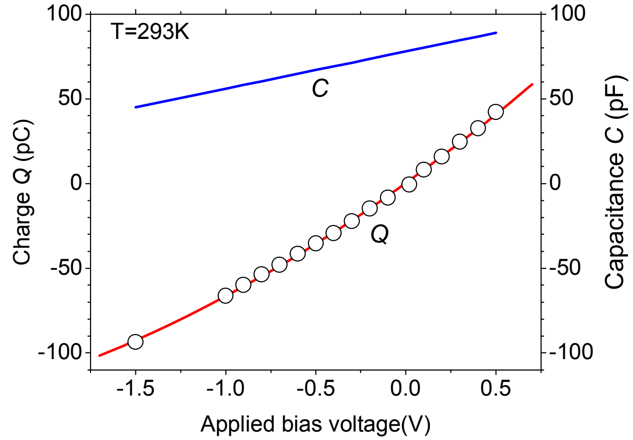

Fig 11: The symbols indicate the charge response Q for varying voltage steps 3 microseconds after the step. The line through these data is a 2 term polynomial fit; the capacitance illustrated is obtained from the analytical derivative using the fitting parameters (IEC-1, 293K, electrode area 8.1×10^{-3} cm^2).

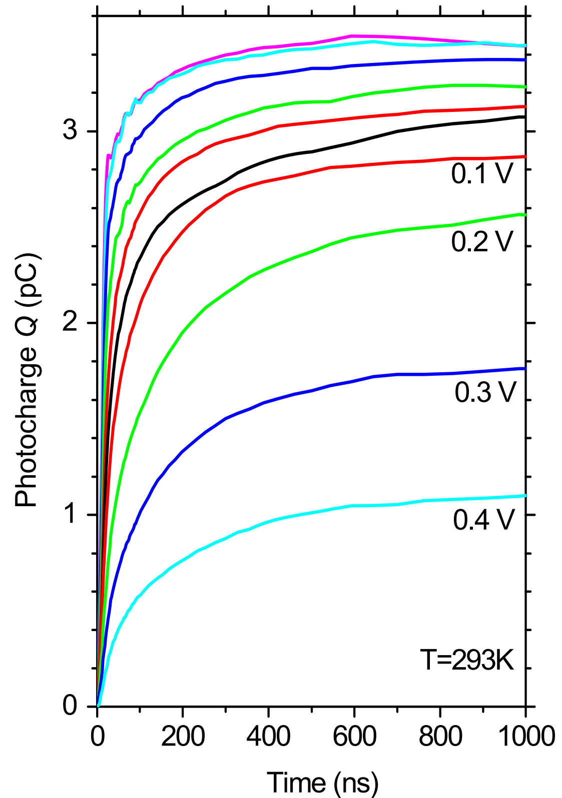

Fig 12: Transient photocharges obtained by integrating the photocurrents at varying bias voltages (-1.0, -0.7, -0.5, -0.2, -0.1…+0.4) (IEC-2, 293K, electrode area of $0.0081 cm^2$).

ns laser pulse. As we mentioned above the laser wavelength was 700 nm, which is strongly absorbed within 10% (about 0.1 μm) of the effective thickness of the sample.

As can be observed the photocharge *Q(t)* rises until it reaches a plateau near 1 μs for all the applied bias voltages. In the simplest examples of photocarrier time-of-flight experiments, the plateau photocharge is voltage-independent, and may be identified with the total photocharge Q_0 absorbed by the sample. For this sample, the photocharge is voltage-dependent. This effect is well known in time-of-flight measurements, where it is usually attributed to "deep-trapping" of the photocarriers [68,69]. In Fig. 13, we have plotted the dependence of the plateau charge on voltage, along with a fitting to the "Hecht" [70] formula:

$$Q = Q_0 \frac{\mu\tau(V_0 - V)}{d^2}\left(1 - \exp\left(-d^2/\mu\tau(V_0 - V)\right)\right) \quad (1)$$

where: $\mu\tau$ is the deep-trapping mobility–lifetime product for holes, d is the width of the structure, and V_0 is an offset voltage related to the built-in potential V_{BI} across the device. As noted earlier, we used the effective, voltage-dependent width obtained from the capacitance for this fitting.

As was expected from the photocharge analysis the plot has two distinct regions:

- At high voltages (fields) the photocharge shows saturation. For these voltages the holes are swept out to the back electrode in less than 1 μs and hence the charge is constant.
- At low voltages (fields) the photocharge depends linearly on the voltage. In this case, holes are being trapped into deeper states for which the emission time is longer than the 1 um integration time for *Q*.

The offset potential V_0 inferred from this fitting (0.49 V) is smaller than the built-in potential V_{BI} for this cell. A lower-limit to V_{BI} (>0.6 V) can be set from the open-circuit voltage *Voc* for this cell.[71] We believe this difference reflects the differing profiles of the built-in potential and the potential induced by the voltage step; in particular, a steep built-in potential profile near the top CdS interface wouldn't be detectible by the photocharge method.

6. Transit Time and Drift Mobility Estimates

The conventional time-of-flight technique measures a transit time t_T required for the mean position of a carrier distribution to move some distance L in a uniform electric field E; the drift-mobility is then defined as $\mu_D = L/(t_t E)$. One implementation of this equation is to identify the transit time as the half-photocharge risetime (the time for the photocharge to reach half its ultimate value Q_0), and then to equate the distance L with half the sample thickness d ($L = d/2$) [72]. For the present research L is equal with depletion width w. Writing $E = (V_0\text{-}V)/w$, the corresponding working equation is:

$$w^2/2t_T = \mu_D(V_0 - V) \quad (2)$$

where again there is an offset expected due to the built-in potential of the cell.

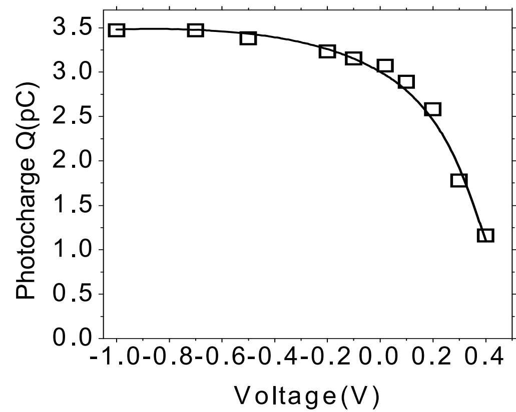

Fig 13: Symbols indicate 293 K photocharge measurements as a function of applied voltage. The line is a fit to the deep-trapping model with parameters Q_0 = 4.57 pC, $\mu\tau = 2.8\times10^{-8}$ cm^2/Vs, and $V_0 = 0.49$ V.

As suggested by eq. (2), in Fig. 14 we have graphed the reciprocal transit-times obtained from the photocharge transients as a function of the size of the voltage step. We estimated w from the capacitance in Fig. 11. Note that w varies somewhat with different voltages; we discuss the size of a systematic error associated with this procedure in an appendix. The transit-time

estimates t_T were obtained from the actual risetimes t_R by making a correction for the electrical response time t_{step} (measured using the voltage step) and the pulse-width of the laser t_{laser}:

$$t_T^2 = t_R^2 - t_{laser}^2 - t_{step}^2 \qquad (3)$$

Details are given in an appendix. The error bars were determined by making several risetime measurements at each voltage and propagating the risetime error into the error in $w^2/2t_T$. The large errors for more negative bias voltages occur because the photocharge risetime approaches the shortest value permitted by the laser pulsewidth and the electronic response time.

The fitting line through these measurements was obtained using a least-square fit; we excluded the two highest voltages for which deep-trapping effects (cf. Fig. 13) are most important. The slope of the fitting line yields a mobility of 0.8 cm^2/Vs. The offset voltage of the fit is 0.30 V. This value is somewhat smaller than found from the deep-trapping analysis (0.49 V); presumably, the discrepancy is indicative of the error in V_0.

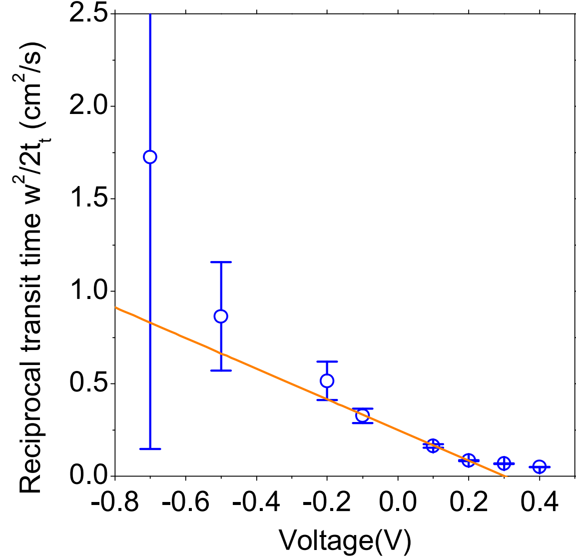

Fig. 14: Dependence of the reciprocal photocharge rise times (293 K) upon applied voltage at room temperature. The fitting line excludes the two points at the largest Voltages. The slope of the linear fit yields the mobility estimate of 0.82 cm^2/Vs. The voltage intercept V_0= 0.303 V is related to the built-in potential V_{BI}.

7. Summary of Mobility Measurements

In Fig.15 we illustrate the summary of the hole drift mobilities as a function of temperature for seven different cells; each substrate is represented by at least two cells, the only exception is substrate IEC-2; this substrate is represented by one cell. Although the measurements as a function of temperature are fairly well-behaved, for nearly every cell we had "outlier" measurements that deviated substantially from the overall trends. We have not traced back this problem. There are also some differences between different cells that were fabricated on the same substrate.

The temperature-dependence is quite weak compared to amorphous semiconductors, and in particular there is no consistent evidence for activated behavior $\mu_D \propto \exp\left(-\Delta E / k_B T\right)$; activated behavior would be expected if the drift-mobility were limited by traps that capture and bind holes with a binding energy ΔE, but release them within the 1 microsecond timescale of our experiments.

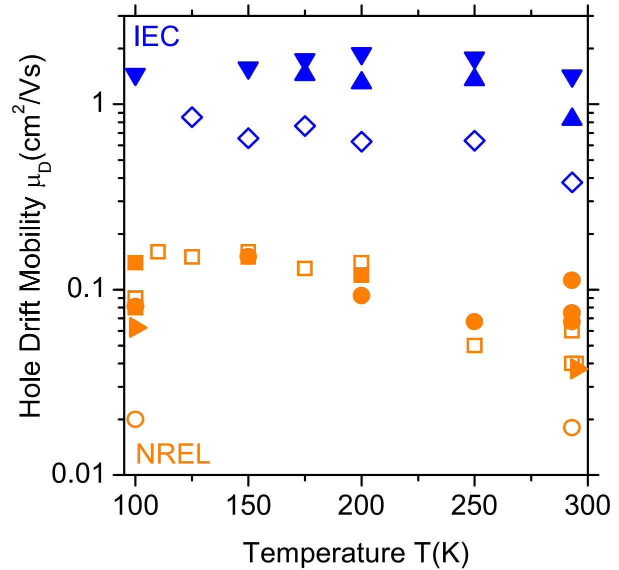

Fig 15: Hole drift mobilities for four CIGS samples at varying temperature. IEC-1: ▲▼. IEC-2:◊. NREL-1: ■□►. NREL-2: ●○

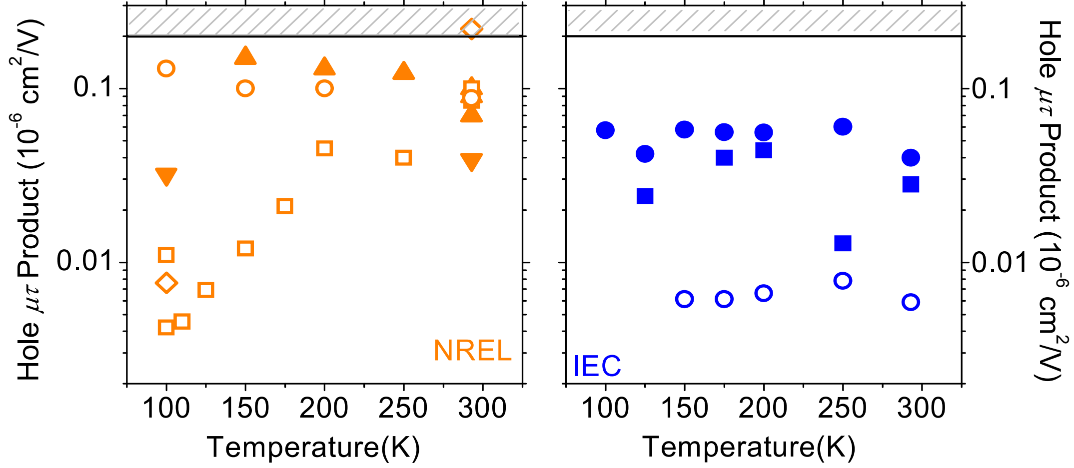

Fig. 16: Variation of the hole deep-trapping mobility-lifetime product $\mu\tau$ with the temperature for various samples. The left panel shows results for NREL devices: □○◊-(NREL-1), ▼▲-(NREL-2); the right panel shows results for the IEC devices: ■●-(IEC-1), ○-(IEC-2).

As we mentioned, there does appear to be significant variation between samples from the two laboratories that is discernible in their drift mobilities, and in the mobility-lifetime products. In Fig. 16 we illustrate the variability of deep trapping mobility lifetime product with respect to temperature; in the left side of Fig 16 we illustrate the NREL cells, and in the right side the IEC cells. Although the measurements as a function of temperature are fairly well-behaved, we had one "outlier" measurement (■ IEC -1) that deviated substantially from the overall trends. We have not traced back this problem. On the other hand, we had an NREL sample which did not exhibit a measurable deep-trapping product at room temperature; we show this inside the shaded rectangular area in Fig.16. This point appears to represents an upper limit to the mobility-lifetime product which can be measured using the Time of Flight method.

8. Discussion

In Fig. 17, we present most of the hole mobility measurements that have been done on the CIGS system using three different techniques: Hall effect, admittance, and time-of-flight. The Hall effect mobilities measured on epitaxial, single-crystal films [61] are much larger than the mobilities for thin-films. Hall effect mobilities in single crystals are usually equated with the fundamental "band mobilities" of carriers in extended electronic states; they are insensitive to trapping effects that could affect the other mobility measurements.

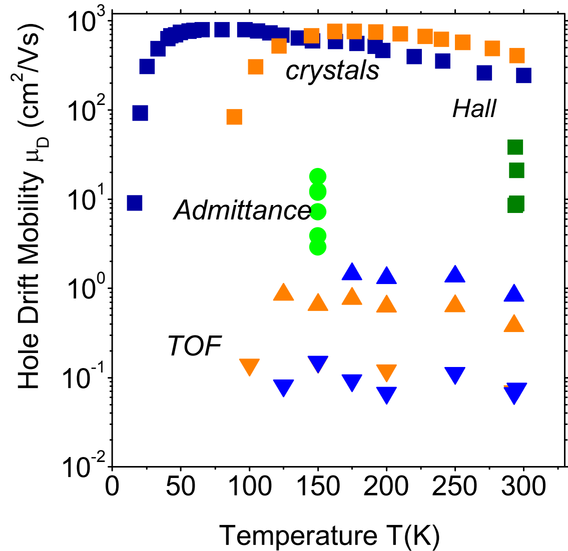

Fig. 17: Survey of hole mobility measurements in CIGS for varying temperatures; samples are thin-films except as noted. ■-Hall effect measurements. ●-Admittance measurements on IEC samples. ▲-IEC TOF measurements, ▼-NREL TOF.

The admittance method mobilities [64] are based on measurements of the dielectric relaxation time $\tau_{dielectric}$ of the bottommost, undepleted region of the thin-films. $\tau_{dielectric}$ is simply related to the region's conductivity $pe\mu$. When the density of mobile holes p in this region can be determined

from analysis of the capacitance, a mobility can be inferred. The fact that the thin-film admittance mobilities are much lower than the single-crystal Hall mobilities indicates that the hole band mobility is greatly depressed in the polycrystalline materials; trapping effects are excluded if the procedure is successful.

The admittance measurements of the hole mobility were done on samples from the Institute of Energy Conversion that are comparable to the samples used to obtain the upper band (▲) of time-of-flight (TOF) mobilities; the TOF mobilities are about ten times smaller. TOF estimates drift-mobilities that are affected by multiple-trapping, so in principle trapping effects could account for the difference. However, given the weak temperature-dependence of the drift-mobilities, we doubt that this explanation is correct for these samples. A second possible origin for the difference in the admittance and TOF mobilities is their differing spatial sensitivities. The TOF technique is sensitive primarily to hole motion in the top half of the depletion layer; the admittance method is sensitive to hole motion in the bottom, undepleted region. We therefore suggest that these samples have a mobility gradient, with larger hole mobilities at the bottom than at the top.

We now turn to the deep-trapping mobility lifetime product ($\mu\tau$) measurements. One earlier experiment reported $\mu\tau_d = 6\text{x}10^{-6}$ cm^2/V for holes in polycrystalline $CuGaSe_2$ [73], which is well above the scale of Fig. 16. The lower values reported here (10^{-8} - 10^{-7} cm^2/V) are just small enough that they could determine the depletion width of illuminated CIGS cells and be a significant factor in their solar conversion efficiencies.

9. Appendices

a. Time-of-flight in a standard depletion layer

When the electric field is not uniform, as evidenced by a voltage-dependent capacitance, the procedure of substituting a depletion width calculated from a capacitance in the expression (2) for the drift mobility leads to a systematic error. The error can be calculated for known field distributions. For example, for the linearly falling electric field of the standard depletion model for semiconductors [74], one can substitute the depletion width for w. We now show that using eq. (2) with this additional assumption leads to overestimation of the drift-mobility by 44%.

We assume that the electric field at the interface is E_0, and that a sheet of carriers is generated at this interface at time $t = 0$. Then the time required for a photocarrier to move a distance x away from the barrier is $t = -(w/\mu E_0)\ln(1 - x/d\, w)$. The "transit time" t_T occurs when $x = w/2$. Since $E_0 = 2(V/w)$, we get $t_T = (w^2/2\mu_D V)0.693$; we are neglecting the built-in potential. Denoting the "naïve" estimate of the drift mobility as $\mu_{D,est} = w^2/2Vt_T$, we obtain $\mu_{D,est} = \frac{1}{.693}\mu_D = 1.443\mu_D$; the naïve expression, uncorrected for the non-uniformity of the field, overestimates the drift mobility by 44%.

We consider 44% to be the upper limit to the systematic error for our measurements; the capacitance we measured (cf. Fig. 11) depended more weakly on voltage than expected for the standard depletion model.

b. Effects of electronic risetimes and laser pulsewidth on transit-time estimation

The risetime of the photocharge convolves several different response times: (i) the photocarrier transit time t_T, (ii) the laser pulsewidth t_{laser}, and (iii) the RC response time coming from the product of the depletion layer capacitance C with the 100 Ohm effective resistance of the electronics (pulser and oscilloscope), and (iv) the dielectric relaxation time of the bottom, undepleted layer of the sample. A rough guide to the effects of (ii), (iii), and (iv) can obtained from the photocharge rise time at large reverse bias (cf. Fig. 11), where the transit time is shorter than the risetime due to the other effects.

However, because the depletion-layer capacitances of the samples increase as the bias voltage increases, this method is not sufficient to estimate the electronic effects for larger (more positive) bias voltages. We also studied the purely electronic effects (iii) and (iv) explicitly by measuring the risetime t_{step} of the charge response of the sample to the bias voltage step. We then calculated the transit time from eq. (3) above, which is based on the Walken and Wallman [75] approximation for convolving risetimes:

$$t_T^2 = t_R^2 - t_{laser}^2 - t_{step}^2 \qquad (3)$$

The laser pulsewidth is 4 ns. We checked this expression using the photocharge risetime t_R at large reverse-bias voltage, where t_T is small, and found satisfactory agreement.

C. Hole Drift-Mobility Measurements and Multiple-Trapping in Microcrystalline Silicon

1. Introduction

There have been several reports of drift-mobility measurements [76- 79] in microcrystalline silicon in the last decade or so since it became clear that this material could be prepared with properties that are interesting for solar cells [80]. There is, of course, an enormous range of possible structures in microcrystalline silicon materials. For each sample there is a spectrum of sizes for the component nano & microcrystallites. Even more poorly understood, for each sample there is also a jumble of non-crystalline material that lies between the crystallites. Unsurprisingly, there has also been a very large spread in reported drift mobilities and transport properties.

In this paper [7,10,11] we shall first summarize our recent hole drift-mobility measurements in a particular form of microcrystalline silicon that has been developed at Forschungszentrum Jülich as a solar cell absorber, and for which cells with 8.7% conversion efficiency have been reported [81]. We shall not offer a detailed defense of the measurements here, nor shall we offer an extended review and comparison with previous work on microcrystalline silicon; these will be presented elsewhere. Instead, we emphasize an unexpected aspect of the present measurements, which is that they exhibit the features of "exponential bandtail multiple-trapping."

Since its first successful application to amorphous semiconductors in the early 1980's (see Tiedje's review [82]), exponential-bandtail multiple-trapping (usually abbreviated as simply "multiple-trapping" or "MT") has become the standard approach to analyzing most transport experiments in hydrogenated amorphous silicon (a-Si:H) and related materials such as amorphous silicon-germanium alloys. The model assumes an exponential bandtail of localized states lying at the bottom of the conduction band, or at the top of the valence band. The application to transport also assumes the existence of a "transport edge," with the property that the only carriers that contribute to electrical transport are those occupying electronic states lying above this edge (for electrons) or below it (for holes); it has generally been assumed that this edge is the "mobility-edge" dividing localized and extended electronic states.

In the present work we have found that multiple-trapping obtains for our measurements in a predominantly crystalline form of microcrystalline silicon. This form of microcrystalline silicon is apparently a far more ordered material than amorphous silicon, and certainly X-ray measurements, Raman scattering, and direct microscopy indicate that most of the volume is associated with small crystallites. One is naturally drawn to models for electrical transport that are based on the effective-mass theory, which would seem to apply at least within a crystallite. Indeed this approach has been applied recently to Hall mobility measurements in *n*-type microcrystalline silicon [83]. It is thus a bit of a shock to discover that the multiple-trapping model taken from amorphous semiconductors is a better description of microcrystalline silicon than is an effective-mass based approach – but this is the implication of our measurements. The multiple-trapping parameters in the microcrystalline material do differ in interesting ways from those that have been reported for a-Si:H, and we shall return to this comparison in the concluding section of this paper.

2. Samples

The samples used for our measurements were *pin* structures prepared in designated chambers of a multi-chamber system using plasma-enhanced chemical vapor deposition at frequencies of 95MHz (VHF-PECVD) [81]. We used ZnO coated glass as a transparent, conductive substrate. The μc-Si:H(B) *p*-layers are about 20nm thick; the films were doped by adding trimethylboron to the silane-hydrogen gas mixture. The intrinsic μc-Si:H layers were prepared using a silane-hydrogen mixture of 5-6%. The n-layer (phosphine doped) was an amorphous a-Si:H(P) layer 30 nm thick. As top contacts we used sputtered ZnO dots with diameters of 1-2 mm; we plasma-etched (SF_6-gas process) the top surface of these structures to remove the n-layer from regions not under the ZnO.

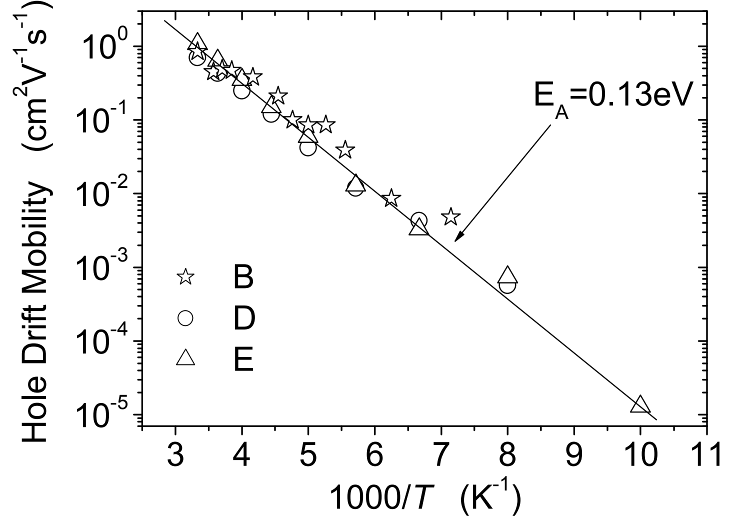

Fig. 18: Hole drift-mobilities measured for three microcrystalline silicon materials (cf. Table I) determined with a displacement/field ratio $d^2/2V = 7.8 \times 10^{-8}$ cm^2/V.

In this paper we present measurements on three samples summarized in Table III. To determine the extent of crystallinity, Raman spectra were recorded from the i-layer at spots right next to the ZnO contacts. The integrated intensity ratio $I_C^{RS} = I_C/(I_A+I_C)$ was determined by deconvoluting the spectra into three signal peaks at 480 cm^{-1}, 500 cm^{-1} and 520 cm^{-1}. The first one can be attributed to a disordered structure like an amorphous phase or grain boundaries (I_A), and the latter two are attributed to the crystalline phase (I_C) [84].

3. Drift-Mobilities

The transient photocurrents were measured in the *pin* diodes following illumination by a 3 ns laser pulse (wavelength $\lambda = 500$ nm) through the *n*-layer. The photocurrent transients were consistent with a conventional interpretation in terms of hole time-of-flight. In particular, the photocharge was independent of the applied voltage, and a transit-time was discernible in the transient. Additionally, the photocurrent at short times was linear in the applied voltage, which is consistent with transport that is linear with electric field.

Table III: Sample Properties

Sample	*Raman Ratio* I_C^{RS}	*i-layer thickness* d (μm)
B	0.71	4.0
D	0.60	3.4
E	0.61	4.3

In Fig. 18 we present our temperature-dependence measurements of the hole drift-mobility for 3 samples [85] corresponding to a particular "displacement/field" ratio $d^2/2V = 7 \times 10^{-8}$ cm^2/V of sample thickness d and applied field (V/d). The activation energy (0.13 eV) is illustrative only, and does not indicate any particular depth for the bandtail traps. These average drift-mobilities, determined using $\mu_D = d^2/(Vt_\tau)$, are much larger than typically obtained in a-Si:H [86], although a direct experimental comparison at the same value for d^2/V is not possible. We compare multiple trapping fitting parameters shortly.

4. Multiple-Trapping Fits

Our procedure for fitting to the multiple-trapping model starts with the transient photocharge $Q(t)$ (the time-integral of the photocurrent $i(t)$). In particular, we fit to the time-dependence of the normalized

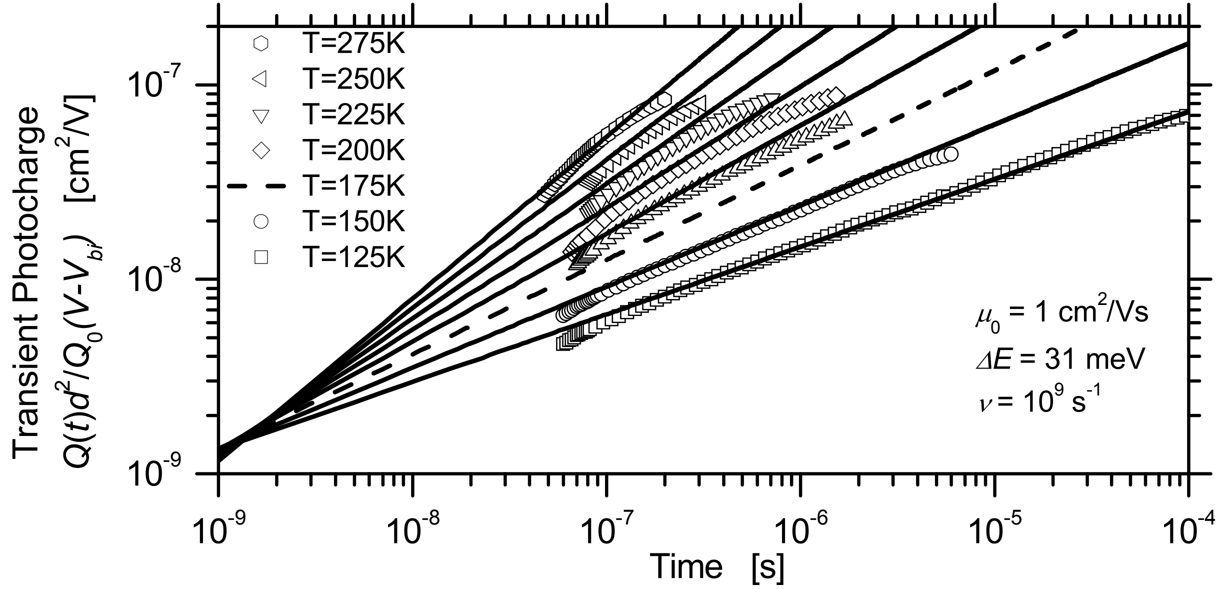

Fig. 19: The symbols are normalized photocharge transients measured in one microcrystalline silicon sample ("D" in Table I); the solid lines are the corresponding calculations using the exponential bandtail multiple-trapping model with the parameters indicated.

photocharge $Q(t)d^2/Q_0(V+V_{bi})$, where Q_0 is the total photocharge of holes generated by the laser pulse, V is the bias voltage, d is the i-layer thickness, and V_{bi} is a correction for the internal field. We have illustrated the photocharge measurements in Fig. 19 for seven temperatures. For clarity, we have removed sections of the transient for $Q(t) > Q_0/2$; these portions of the transient are past the "transit time," and are not used in our multiple-trapping fitting procedure. We have also removed early-time portions of the transients that are clearly dominated by response-times of the measurement.

The solid lines in Fig. 19 are the multiple-trapping fittings. The actual equation that was fitted to the normalized photocharge is [86]:

$$L(t)/E = K\left(\mu_0/\nu\right)(\nu t)^{\alpha(T)}. \qquad (1)$$

$L(t)$ is the mean displacement for photocarriers after a delay time t and with electric field E. The dispersion parameter $\alpha = kT/\Delta E_V$, where ΔE_V is the width of the exponential, valence bandtail, μ_0 is the valence band-mobility, and ν is an "attempt-to-escape" frequency characterizing the rate of release of holes from the bandtail traps. The constant $K = \sin(\alpha\pi)/(\alpha\pi(1-\alpha))$ is of order unity. The multiple-trapping parameters we chose (and that are the basis for the solid lines shown in Fig. 2) are given in Table IV below, along with some results for a-Si:H [86,87].

Table IV: Multiple-trapping fitting parameters

Multiple-trapping parameter	*μc-Si:H* (this work)	*a-Si:H* (ref. 86)	*a-Si:H* (ref. 87)
Valence band-mobility μ_0 (cm^2/Vs)	1.0	0.7	0.3
Bandtail width ΔE_V (meV)	31	45	48
Attempt-frequency ν (s^{-1})	$9x10^8$	$1x10^{12}$	$8x10^{10}$

5. Meaning of Multiple Trapping in Microcrystalline Silicon

One approach to analyzing mobilities in polycrystalline materials is to invoke the effective masses that would obtain for electrons and holes in the single crystal, and assume that the grain boundaries act as scatterers or barriers and as the locus for traps for the carriers [83]. It is instructive to use this approach crudely to calculate an "effective-mass carrier mobility" for holes $\mu_h^{e.m.}$ utilizing the expression $\mu_h^{e.m.} = v_{th} l / (kT/e)$, where v_{th} is the "thermal velocity" for holes (about 10^7 cm/s in c-Si near room-temperature) [88] and l is a scattering length. If the scattering length is identified with a typical crystallite size of 3 nm, we infer $\mu_h^{e.m.} = 120$ cm^2/Vs, or about 100 times larger than the estimate in Table I. The effects of traps and barriers seem unlikely to explain the discrepancy for our samples, since these were already (implicitly) incorporated in the analysis that led to the estimate $\mu_0 = 1$ cm^2/Vs.

We suggest that, for our samples of microcrystalline silicon, the disorder is sufficient to strongly alter the bandedge states from their crystalline counterparts. In particular, we suggest that the bandedge states of the crystal have been transformed into a bandtail (i.e. that the density-of-states $g(E)$ has been altered), and that a *mobility-edge* has formed within the bandtail [89] (i.e. states lying deeper in the energy gap are localized).

The mobility-edge has been widely applied to amorphous semiconductors [82,90], and has recently been applied to microcrystalline samples with a larger fraction of amorphous "tissue" [91]. Here we are suggesting that it be applied to samples that are predominantly crystalline. In the mobility-edge model, hole states with energy levels below the mobility-edge ($E < E_V$) are completely delocalized (by definition), although with very different wavefunctions than the effective-mass states of crystals. Hole states lying above the mobility-edge ($E > E_V$) are localized. Both analytical and computational studies of mobility-edges [92,93] indicate that the localization radius for a hole state grows very rapidly, and may even diverge, as the state's energy approaches the mobility-edge. It isn't clear theoretically how particular atomic-scale features such as "strained bonds" are incorporated into the bandtail states.

With this perspective, we first discuss the bandtail width ΔE_v. The estimate of 31 meV for the microcrystalline material seems unremarkable in the context of work on holes in amorphous silicon, which yield values in the range 40 – 50 meV. It is worth noting that disorder affects holes and electrons very differently. The conduction bandtail in amorphous silicon has a width around 22 meV [82,90]. Electron properties in samples quite similar to the present ones have been studied using post-transit time-of-flight [91]; bandtail multiple-trapping did not apply for these transients. An interesting possibility is therefore that electron transport may be governed by effective masses in exactly the same material for which holes require a mobility-edge approach.

The fact that the hole band-mobility μ_0 is about the same in the present microcrystalline samples and in amorphous silicon seems to support the mobility-edge interpretation, and more broadly suggests that a value near 1 cm^2/Vs may be a universal property of a mobility edge. Such "universality" is also suggested by the fact that electron band-mobilities in amorphous silicon are also around 1 cm^2/Vs [82,90]. Interestingly, a band mobility of 1 cm^2/Vs is *not* an obvious implication of the existing theoretical treatments of mobility-edges.

Finally, we turn to the attempt-frequency ν. It is quite interesting that the value for microcrystalline silicon is substantially (about 100 times) smaller than the lower values reported for a-Si:H. However, even for a-Si:H, there is no well-accepted physical interpretation for this parameter. One often-mentioned interpretation is that ν be identified as a "typical phonon frequency," but this association fails to explain either the very low magnitudes or the enormous range of magnitudes that have been reported experimentally [94]. Yelon and Movaghar have suggested that multi-phonon effects lead to the variations, and this perspective has been applied by Chen, *et al.*, to drift-mobility measurements [95]. Another possibility originating with high-field drift-mobility measurements in a-Si:H has been that ν reflects the bandedge density-of-states $g(E_V)$ [96], which suggests that the present measurements be interpreted as indicating a substantially lower value for $g(E_V)$ in microcrystalline than in amorphous silicon. Plainly, we need more clues from experiment about the meaning of this parameter; it seems possible that its dramatic lowering in microcrystalline silicon could be providing it.

D. Polyaniline heterojunction diodes

1. Introduction

Organic/inorganic heterostructure solar cells have been studied by various groups in the past. Among those studies, there were only a few reports on conducting polymer/amorphous silicon (a-Si:H) structures [97-99] and conducting polymer/crystalline silicon (c-Si) structures [100,1] In this paper, we report our research on polyaniline (PANI)/a-Si:H heterostructure solar cells; PANI is a *p*-type conducting polymer and is stable in the air, making it suitable for various applications. We studied the open-circuit voltage V_{OC} of these heterojunctions under illumination as a function of the conductivity of the PANI films. The measurements are consistent with the model that V_{OC} was limited by the work functions of the PANI. We compare these results with our recent work on PANI/c-Si cells [1]. For these cells, V_{OC} vs. conductivity data shows essentially the same relation as for a-Si:H - excepting that V_{OC} saturates at 0.5 V for higher conductivity PANI. The band offsets between a-Si:H and c-Si were estimated using the two sets of measurements, and were in satisfactory agreement with previous estimates from photoemission measurements [101,102] We discuss the saturation effect for c-Si/PANI cells in light of the absence of saturation for the a-Si:H/PANI cells.

2. Experimental Procedures

Dispersions of acid-doped PANI in xylene from Sigma-Aldrich, Inc. and from Ormecon GmbH [103] were used. *n-i* a-Si:H structures were deposited onto stainless steel using a commercial plasma-enhanced chemical vapor deposition reactor. The thickness of the intrinsic layer is 0.80 μm. *n*-type, (100) crystalline silicon wafers were etched by 2.5% HF solution; the wafer conductivities were 2 S/cm. For most cells, aluminum was evaporated on the unpolished backs of the c-Si wafers to form a back contact. On some cells, *n*-type a-Si:H was deposited at NREL to form a back surface field contact.

The two different solar cell structures were then made by spin coating the PANI dispersions onto freshly made a-Si:H or the polished surface of c-Si. A wide range of PANI conductivities was obtained by increasing the concentration of xylene of the Aldrich dispersion. The films were dried in air at 80 C for 24 hours after casting for Aldrich's PANI and at 100 C for 1 min for Ormecon's PANI. A 1 mm diameter gold contact (50 nm thick) was evaporated onto the PANI film. The area of the PANI film was typically about 1 cm^2. The PANI films were 0.1-0.4 μm thick [104]; the conductivity of the PANI films was between 10^{-5} S/cm to 10^1 S/cm depending on dilutions for the Aldrich dispersion, and was 10^2 S/cm for the Ormecon dispersion. Scanning electron microscopy indicated that the films were continuous, although with somewhat differing morphologies for the differing dilutions.

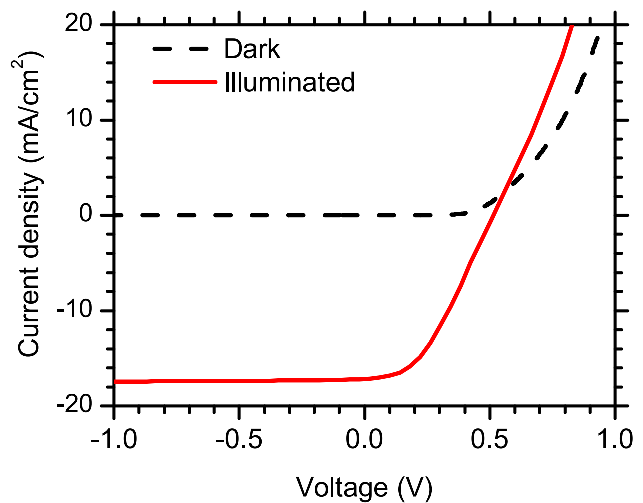

Fig. 20: Current density as a function of voltage across a PANI/c-Si diode (Ormecon dispersion, 1.2×10^2 S/cm). The white-light illuminator intensity was 0.1 W/cm2.

3. Results and Discussion

The dependence of the current density upon voltage is shown in Fig. 20 for a PANI/*n*-Si diode (Ormecon dispersion) for the dark and for tungsten-halogen illumination through the PANI (intensity 0.1 W/cm^2). The saturated photocurrent density is 17 mA/cm^2, which is reasonably consistent with the photon flux that reaches the c-Si after filtering by the PANI film. The open-circuit voltage V_{OC} is 0.51 V, which is about 0.1 V below the values observed for c-Si

based cells with metal back electrodes [105]. The low fill-factor of 41% is due to the lateral resistance of the PANI film (and the absence of a top metallic grid). It is of interest that the light and dark curves cross at about 0.6 V; while such "crossover" is not typical of homojunction c-Si diodes, it has been reported previously for heterojunctions such as PEDOT/a-Si:H [97,99].

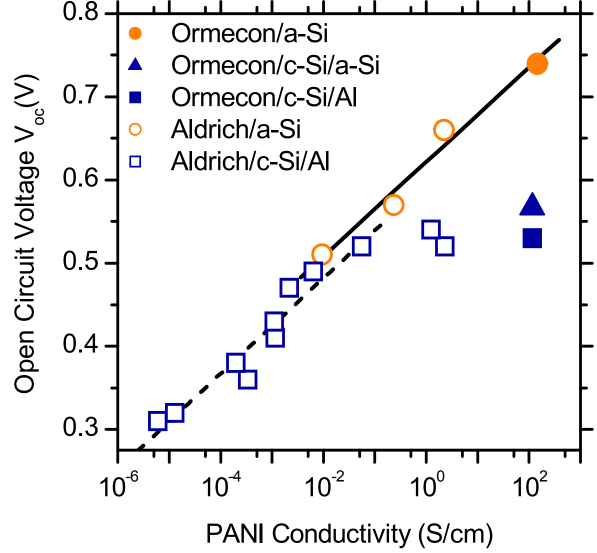

Fig. 21: Open-circuit-voltages V_{OC} of PANI/a-Si:H and PANI/c-Si solar cells for PANI films with widely varying conductivity. The white-light illumination intensity was 0.58 W/cm^2. The legend indicates the source of the PANI and also the back contact for the c-Si structures.

In Fig. 21, the open-circuit-voltages V_{OC} for the PANI/a-Si:H and PANI/c-Si diodes are shown as a function of the conductivities σ of "sibling" PANI films cast onto glass using the same dispersion. We used white-light illumination through the PANI with intensity 0.58 W/cm^2.

For c-Si diodes, V_{oc} was almost constant (at V_{OC}^{sat} = 0.52 V) above a threshold conductivity σ_c = 0.05 S/cm. Below the threshold conductivity, the data can be fitted well by the form:

$$V_{oc} = 0.72 + (k_B T/e)\ln(\sigma/\sigma_{\max}) \ , \quad (1)$$

where $k_B T/e$ = 0.025 V is the ratio of the Boltzmann thermal energy to the electron charge and $\sigma_{\max}$ is 10^2 S/cm, which is the largest conductivity PANI (from Ormecon) that we used. For $\sigma < \sigma_c$, the logarithmic dependence of V_{OC} on PANI conductivity is consistent with the idea that V_{OC} is limited by the built-in potential across the PANI/c-Si heterojunction [106]:

$$eV_{oc} \approx eV_{BI} = E_F^{\mathrm{Si}} - E_F^{\mathrm{PANI}} \ , \quad (2)$$

where E_F^{Si} is the Fermi-level of the (n-type) c-Si and E_F^{PANI} is the Fermi level of the p-type PANI film. Assuming that the conductivities of the PANI films are mainly determined by their Fermi levels, we write

$$\sigma = \sigma_{00} \exp\left(-\left(E_F^{\mathrm{PANI}} - E_V^{\mathrm{PANI}}\right)/k_B T\right) , \quad (3)$$

where E_V^{PANI} is the transport level energy for holes in the PANI films. We obtain for V_{OC} (in the built-in potential limit) that:

$$eV_{OC} = \left(E_F^{\mathrm{Si}} - E_V^{\mathrm{PANI}}\right) - k_B T \ln(\sigma_{00}/\sigma) \ . \quad (4)$$

Eq. (4) accounts for measured slope 0.026 V of the dependence of V_{OC} upon the natural logarithm of the film conductivity.

We checked that Eq. (3) does describe the temperature-dependent conductivities of our films. The results are presented in Fig. 22, which shows that lower conductivity films have larger activation energies. The fitting curves roughly converge at a negative "Meyer-Neldel" temperature $T_{MN} \approx$ -180 K and a conductivity $\sigma_{\mathrm{MN}} = 2\times10^2$ S/cm. Inverse Meyer-Neldel behavior (i.e., negative values for T_{MN}) is typically observed when the (temperature-dependent) Fermi-level lies in a bandtail region [107]. Assuming that σ_{MN} estimates the fundamental bandedge conductivity σ_{00} [108], we can use Eq. (4) to infer the difference in energy levels between Fermi level in the c-Si and the hole transport level of the PANI; the result $E_F^{\mathrm{Si}} - E_V^{\mathrm{PANI}} = 0.74$ eV is consistent with work function estimates in heavily doped PANI [109].

For a-Si:H, the data can be fitted fairly well by eq.(1) over the entire range of PANI conductivities, including conductivities for which the c-Si voltage was saturated. These results indicate that the saturation effect is not due to any intrinsic limitation of the PANI. Because the a-Si:H is part of an *nip* structure, the idea that V_{OC} is limited by the built-in potential V_{BI} must be modified. We shall interpret eV_{OC} as a measurement of the difference between the Fermi level of the PANI and the *electron quasi-Fermi level* E_{Fn} of the intrinsic a-Si:H under illumination. Device-modeling studies of a-Si:H solar cells suggest that the *n/i* interface of illuminated a-Si:H *pin* cells acts essentially as an ideal contact to E_{Fn}, so V_{OC} will mainly be determined by properties of the *p/i* interface [110].

In Fig. 23 we illustrate these 2 differing approaches to understanding the limitation of V_{OC} by the PANI work function. Fig. 23 is drawn for a particular PANI conductivity of 0.01 S/cm. The conductivity of the n-type silicon wafer was 0.5 S/cm, which corresponds to a Fermi level E_F lying 0.25 eV below the conduction bandedge E_C through the textbook result $\sigma = N_C e \mu_n \exp\left(-\left(E_C - E_F\right)/kT\right)$.

For a-Si:H, we estimate from our device modeling that the electron quasi-Fermi level E_{Fn} of the intrinsic layer is 0.30 eV below E_C. (under illumination of 0.6 W/cm^2) [110]. As can be seen from the figure, this analysis implies particular values for the conduction and valence band offsets between c-Si and a-Si:H. We obtained a conduction band offset between the two materials of 0.08 eV. Using bandgaps of 1.12 eV for c-Si and 1.75 eV for a-Si:H, the valence band offset is 0.55 eV. Many values for the valence band offset between a-Si:H and c-Si interface have been reported; our estimate of 0.55 eV seems reasonably consistent with the relatively recent measurements of 0.44eV±0.02 eV from photoemission experiments [101,102].

A related experiment on the effects of varying the doping level of a *p*-layer on a-Si:H *pin* structures was reported by Dawson, et al. [111] who used boron-doped a-Si:H. In their experiment the values for V_{OC} were somewhat larger (about 0.8 V) than our largest value, and they had little dependence on the doping levels of the p-layer. We suspect that this qualitative difference between their results with a-Si:H:B and the present work with PANI has to do with the much lower conduction band level in a-Si:H compared to PANI.

We now return to the following feature of Fig. 21. For c-Si, V_{OC} values saturated near 0.5 V for PANI conductivities that exceeded about 0.1 S/cm. However, for a-Si:H V_{OC} increased continuously with increasing PANI conductivity. We have considered several mechanisms for the saturation seen in c-Si. Poor quality c-Si that intrinsically limits V_{OC} is one possibility that we have previously excluded. In the present work, we compared V_{OC} for two different back contacts: evaporated Al, and n-type a-Si:H (a "back surface field" contact). As can be seen in Fig. 21, the improvement obtained by using a-Si:H is about 0.03 V. The improvement is significant, but Fig. 21 suggests that a much larger improvement is still possible, In particular, the data suggest that the intrinsic properties of the highest conductivity PANI (from Ormecon) are able to support a V_{OC} as large as 0.7 V in c-Si, as they do for the a-Si:H/PANI cells.

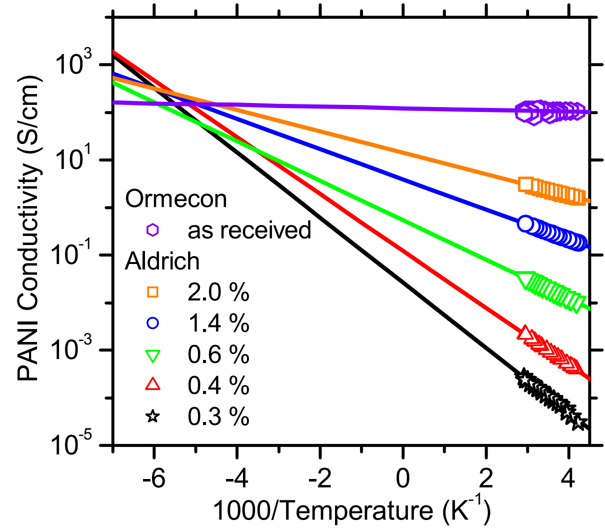

Fig. 22: Conductivity measurements as a function of reciprocal temperature 1000/*T* for six PANI films cast onto glass from dispersions with differing dilutions. The percentages indicated in the legend are the weight percentages of PANI in xylene. While the measurements for each sample show simple activated behavior, the fitting lines converge at a negative Meyer-Neldel temperature T_{MN} = -180 K.

V_{OC} saturation thus suggests to us that the PANI Fermi level at the c-Si interface is "pinned" at an energy higher than its bulk Fermi level. This pinning apparently doesn't occur for a-Si:H, which is a clue as to the underlying physical mechanism. One mechanism that we have been considering for the V_{OC} saturation is "electrophoresis" of charged molecules in the PANI films near the interfaces that might lead to dedoping of the film. However, we can estimate the electric fields near the interface for c-Si and for a-Si:H using elementary models. For c-Si with a conductivity of 0.5 S/cm, and V_{BI} of about 0.8 V across the diode, the interface electrical field in the dark is about 10^4 V/cm. The value for the interface field that we estimate for a-Si:H in the dark is about the same. It thus seems unlikely that the electrophoresis mechanism is correct; we are still seeking a better model.

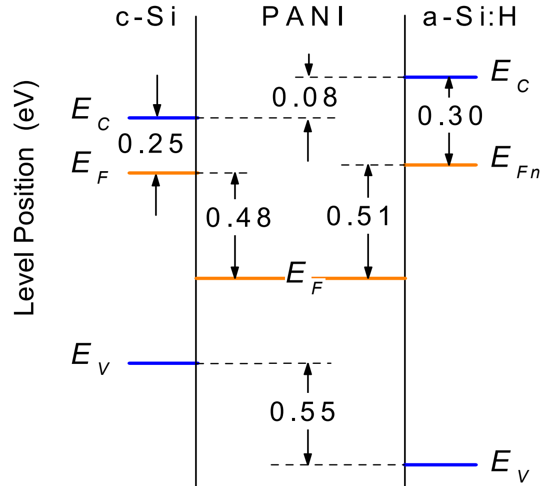

Fig.23. Proposed alignments of Fermi levels and bandedges in c-Si, PANI, and a-Si:H; conductivities and illumination levels are indicated in the text. Note that the analysis yields c-Si/a-Si:H conduction and valence band offsets of 0.08 and 0.55 eV, respectively.

4. Conclusions

The dependence of open-circuit-voltages V_{OC} for PANI/a-Si:H and PANI/c-Si structures was studied for varying PANI conductivities. Generally, the open-circuit voltage V_{OC} increases with increasing PANI conductivity as expected when V_{OC} is limited by the work function of the PANI film; an analysis based on this idea yielded band offsets that are consistent with more direct measurements such as photoemission. For a-Si:H, the V_{OC} values for the highest conductivity PANI (about 0.75 V) are lower than obtained with Si-based *p*-layers, and we consider it unlikely that PANI *p*-layers are of technological significance for a-Si:H. For c-Si, V_{OC} saturated at about 0.5 V for PANI conductivities greater than 0.1 S/cm. The saturation mechanism is not understood, and it may be possible to achieve higher V_{OC} values comparable to the highest reported with other *p*-type materials.

E. Infrared Interface Spectra in Cells

For the last few years we have been developing an infrared modulation spectroscopy technique that probes the optical spectra of dopants and defects at the critical interfaces between the layers of amorphous silicon *pin* solar cells [112- 115]. In brief, the reverse bias voltage across a cell is sinusoidally modulated, and the corresponding modulation of an optical transmission is detected. We illustrate such a spectrum as Fig. 24, where the modulation spectrum $\Delta T/T$ of the optical transmission through a *pin* solar cell is shown. The principal feature in this spectrum is the large peak near 1.85 eV; this feature, which depends upon the magnitude of the DC potential V_{DC} across the cell, is due to the well-known *electroabsorption* effect in the intrinsic, a-Si:H layer of the cell [116]. The much weaker infrared signal is nearly independent of V_{DC}, and is attributed to the change in optical transmission as the *charge state* of dopants and defects near the interfaces is modified by the sinusoidal modulation of the electric potential across the cell. The electroabsorption effect is quadratic in electric field, which leads to a signal quadratic in the modulated field and V_{DC}. The interface effect varies with the charge modulation at the interfaces, and is independent of V_{DC} when the capacitance is also independent of V_{DC}.

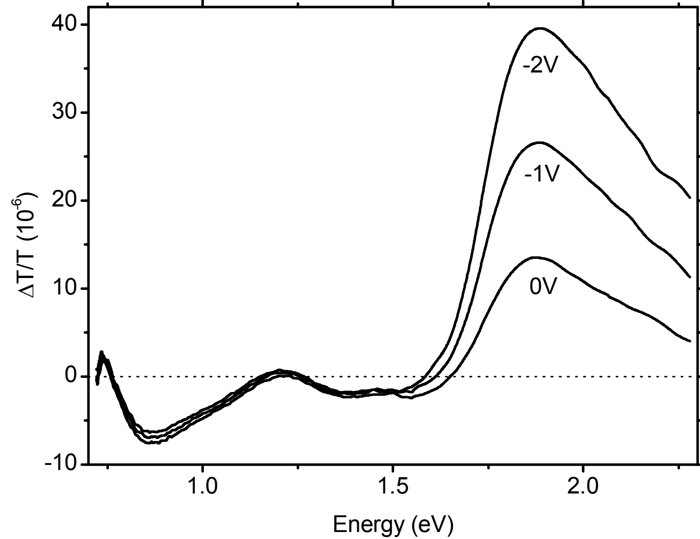

Figure 24: Transmittance modulation spectrum $\Delta T/T$ for an amorphous silicon-based *pin* solar cell prepared at BP Solar. Spectra were taken under three different DC reverse bias voltages (V_{DC}) as indicated. The larger, voltage-dependent peak near 1.85 eV corresponds to the well established *interband electroabsorption*, and depends linearly on V_{DC}. The weaker infrared response is due to charging and discharging of dopant and defect levels near the *n/i* and *p/i* interfaces, and shows little dependence on V_{DC}. Sample with 3% phosphorus doping level. Measured with 400Hz, 1.0 V_{pp} modulation.

In work supported by this subcontract, we studied a series samples with varying phosphorus-doping level in the *n*-layer [117]. We found, for high doping levels (1% - 5%), a sharper spectral line near 0.75 eV with a width of 0.1 eV. This line is nearly absent in lower doping (below 1%) samples. We have previously attributed this line to the internal optical transitions of a "P_4D" complex incorporating both a fourfold-coordinated phosphorus atom (P_4) and a dangling bond (D) [113,118]. We have analyzed the present measurements to estimate the relative concentrations of "standard" dopant atoms P_4 (ie. those not in complexes) and dopant complexes P_4D. We are unaware of previous experimental estimates of this ratio, and we believe that they show the utility of infrared charge-modulation spectroscopy for interface studies. Our measurements are broadly consistent with the predictions of the model for doping developed by Street, although the measurements differ from this model in detail.

In this experiment, we measured the transmittance modulation spectra for a series of samples of phosphorus-doped amorphous silicon (a-Si:H:P) layer with gas-phase doping levels between 0.17% - 5%. These samples were made as a sequence at BP Solar; the substrate for each deposition was glass coated with textured SnO_2. The *p*-type layer deposited onto the SnO_2 was a-SiC:H:B, followed by a-Si:H and by *n*-type a-Si:H:P. Sputtered TCO was applied to the top and used as the electrical contact. The intrinsic layers were around 200 nm thick as inferred from capacitance measurements. A buffer layer was deposited between *p*-type and intrinsic layers.

Fig. 25 shows the infrared charge-modulated transmittance spectra ΔT/T for samples with the indicated doping levels. Each spectrum has been normalized by its peak amplitude. We first noticed that for samples with doping levels below 1% there is a negative, broad peak in the modulation spectrum near 0.85 eV. We attribute this spectrum to occupancy modulation of isolated dopant atoms in the *n* and *p* layers; similar spectral features have been reported in photomodulated transmittance spectra of phosphorus-doped a-Si:H. We exclude the photodetachment of electron from D^- as possible source for this negative absorption spectrum. This is because the Fermi energy is at most 0.2 eV below conduction band, but D^- is located 0.9 eV deep below conduction band. Depletion of such a deep level should be negligible. This argument is also supported by the frequency-independent spectrum with modulation frequency range from 200 Hz to 20kHz, although we won't show this here.

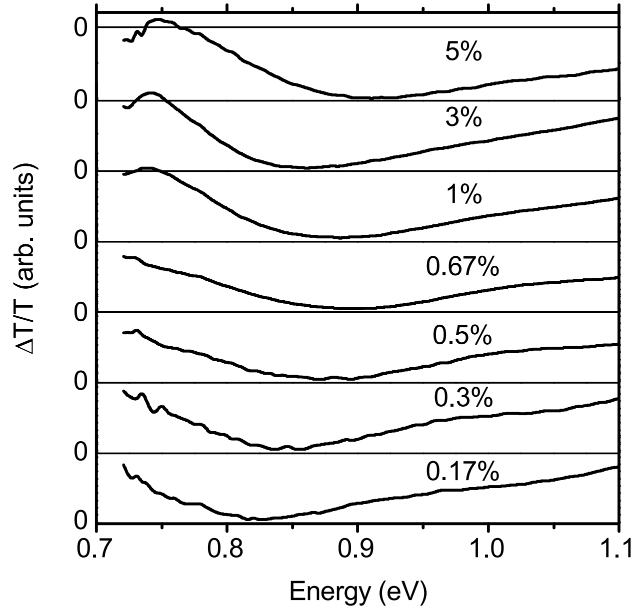

Fig. 25. Normalized modulated infrared absorption spectrum. Samples were prepared at BP Solar with varying phosphorus doping levels (from 0.17% to 5% as indicated). At higher doping levels (1% and above), there is a line spectrum at 0.75 eV of about 0.1 eV wide. This line is essentially absent in samples with doping levels below 1%. This sharp line indicates the internal optical transitions of a complex incorporating four fold coordinated phosphorus and a dangling bond.

At high doping levels (1% and above), we find a sharper, positive peak at 0.75 eV with a width of 0.1 eV. This line is nearly absent in low doping samples. The existence of a sharp absorption line suggests transitions between the ground state and a localized excited state of some center in phosphorus-doped a-Si:H. In our previous work we suggested the possibility that P_4D complexes are responsible for this spectral feature [113]. Positron annihilation measurements [118] are also consistent with complexing at high doping levels. Fig. 26 shows a simple possible level diagram for a P_4D complex, and corresponding absorption spectrum for an internal optical transition. As we can see from figure 3, when the Fermi energy is lowered, the depletion of P_4D states near band edge promotes the internal transition to these states from deeper complex states.

Street [119] has previously noted that formation of P_4D complexes is favored at high doping levels, while lower doping levels favor the formation of uncorrelated P_4 and D-centers in essentially equal concentrations. In the next a few paragraphs, we will discuss briefly, based on samples studied in this paper, about the doping models proposed by Street [119]. The standard doping model involves nearly equal densities dangling bonds (D centers) and of phosphorus atoms bonded to four silicon atoms (P_4 centers). The corresponding densities can be represented by [119]

$$N_{P_4} = N_D = \left(K_S N_{Si_4}\right)^{1/2} \left(N_{P_3}\right)^{1/2} , \qquad (1)$$

where K_S is the rate constant and P_3 denotes a phosphorus atom with threefold coordination. The concentrations of pairs depends linearly on phosphorus concentration [119]:

$$N_{pair} = K_P N_{Si_4} N_{P_3} = \left(K_P N_{Si_4}\right)\left(N_{P_3}\right), \qquad (2)$$

where K_P is the rate constant for pair generation. Low P densities favor isolated P_4 and D centers; higher densities favor complexing.

To analyze our spectra, we assumed that the two spectral features (broad/negative, and narrow/positive) in Fig. 25 originate with P_4 and P_4D configurations. We fit the infrared spectrum with two Gaussian peaks. Fig. 27 shows a typical fitting result for the sample made with 3% P. The dashed line represents the positive peak; the dotted line represents the negative peak. As can be seen, the sum of these two spectrum peaks (the solid line in the figure) fits the actual spectrum quite satisfactorily. We plotted the ratio of the strengths of these two spectral lines for all of our samples as the open symbols in Fig. 28. We believe that this value is proportional to the ratio of the densities of the two types of dopant configurations.

From Eq. 1 and 2, we calculate the ratio of concentrations as:

$$N_{pair} \big/ N_{P_4} = \left(K_P \big/ K_S\right)\left(N_{Si_4}\right)^{1/2}\left(N_{P_3}\right)^{1/2} . \qquad (3)$$

We fitted the resulting proportionality (to $P^{1/2}$) to the measurements in Fig. 28. The fitting accounts fairly well for the dependence of the ratio of spectral line strengths upon the phosphorus concentration, and thus supports to some degree our identification of the two spectral features. There does appear to be sharper structure near a “critical” phosphorus level of 1% that is not reproduced by the fitting, and we hope that further measurements will clarify this possibility.

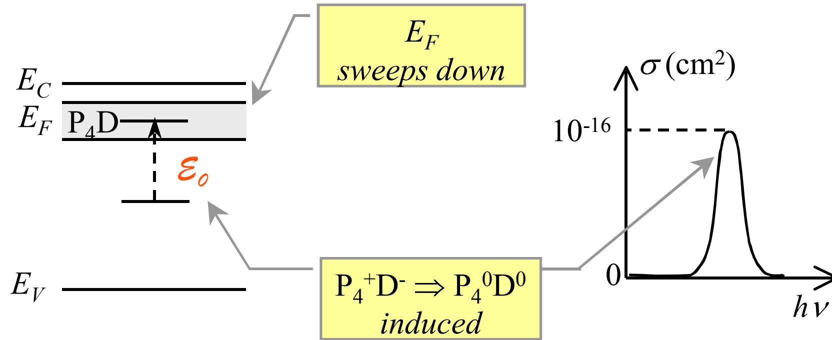

Fig. 26. Optical effects resulting from a change in the Fermi energy in heavily phosphorus doped a-Si:H (probably at doping level of 1% and above). The drawing on the left indicates an internal electron excitation from a deep level to a shallower level of a complex, which incorporats four fold coordinated phosphorus and a dangling bond. The depletion of occupied states near the band edge of a-Si:H, as the Fermi energy is lowered, induces this internal transition, which account for a sharp, positive absorption spectrum.

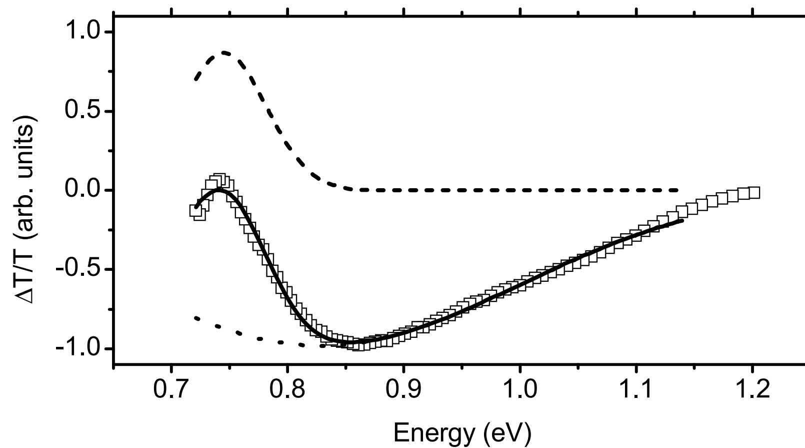

Figure 27: Spectrum analysis. Fit infrared spectrum with two Gaussian spectrum peaks. Symbols indicate the measurement; lines indicate the fitting results (dashed: positive Gaussian peak t 0.75 eV; dotted: negative Gaussian peak at 0.84 eV; solid: sum of these two peaks).

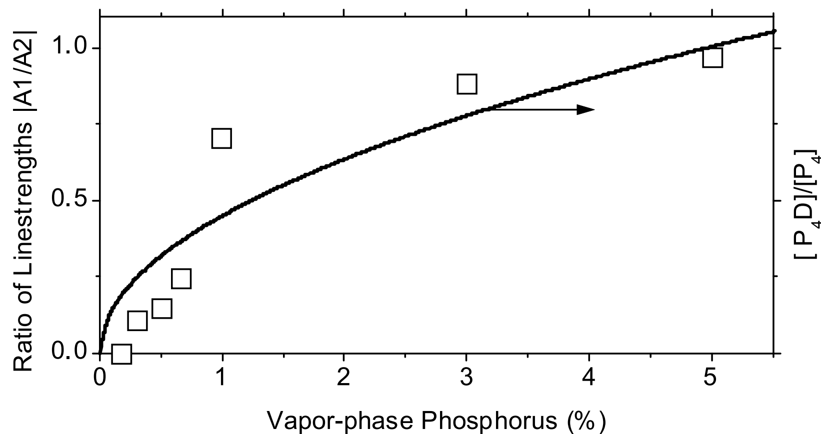

Figure 28: Relative peaks strength. Symbols indicate the ratio of the strength of the positive peak over that of the negative peak. Line indicates the fitting result of Eq.3 in text. The fitting coefficient was 4.5.

References

1. “Polyaniline on crystalline silicon heterojunction solar cells,” Weining Wang and E. A. Schiff, *Appl. Phys. Lett.* **91**, 133504 (2007). DOI: 10.1063/1.2789785.

2. "Hole Mobilities and the Physics of Amorphous Silicon Solar Cells," E. A. Schiff, *J. Non-Cryst. Solids* **352**, 1087-1092 (2006).

3. "Hole Mobility Limit of Amorphous Silicon Solar Cells," Jianjun Liang, E. A. Schiff, Baojie Yan, J. Yang, *Appl. Phys. Lett.* **88** 063512 (2006).

4. "Conducting polymer and hydrogenated amorphous silicon hybrid solar cells," E. L. Williams, G. E. Jabbour, Q. Wang, S. E. Shaheen, D. S. Ginley, and E. A. Schiff, *Appl. Phys. Lett.* **87**, 223504 (2005).

5. “Low Mobility Solar Cells: A Device Physics Primer with Application to Amorphous Silicon,” E. A. Schiff, *Solar Energy Materials and Solar Cells* **78**, 567-595 (2003).

6 "Bandtail Limits to Solar Conversion Efficiencies in Amorphous Silicon Solar Cells," K. Zhu, J. Yang, W. Wang, E. A. Schiff, J. Liang, and S. Guha, in *Amorphous and Nanocrystalline Silicon Based Films - 2003*, edited by J.R. Abelson, G. Ganguly, H. Matsumura, J. Robertson, E. A. Schiff (Materials Research Society Symposium Proceedings Vol. 762, Pittsburgh, 2003), pp. 297--302.

7. "Hole Drift Mobility Measurements in Microcrystalline Silicon," T. Dylla, F. Finger, and E. A. Schiff, *Appl. Phys. Lett.* 87, 032103 (2005).

8. "Light-soaking Effects on the Open-circuit Voltage of Amorphous Silicon Solar Cells," J. Liang, E. A. Schiff, S. Guha, B. Yan, and J. Yang, in *Amorphous and Nanocrystalline Silicon Science and Technology – 2005*, edited by R. Collins, P.C. Taylor, M. Kondo, R. Carius, R. Biswas (Materials Research Society Symposium Proceedings Vol. 862, Pittsburgh, 2005), A13.6.

9. "Temperature-dependent Open-circuit Voltage Measurements and Light-soaking in Hydrogenated Amorphous Silicon Solar Cells," J. Liang, E. A. Schiff, S. Guha, B. Yan, and J. Yang, in *Amorphous and Nanocrystalline Silicon Science and Technology – 2005*, edited by R. Collins, P.C. Taylor, M. Kondo, R. Carius, R. Biswas (Materials Research Society Symposium Proceedings Vol. 862, Pittsburgh, 2005), A21.8.

10. "Drift-mobility measurements and mobility-edges in disordered silicons," E. A. Schiff, J. Phys.: Condens. Matter **16**, S5265-5275 (2004).

11. "Hole Drift-Mobility Measurements and Multiple-Trapping in Microcrystalline Silicon," T. Dylla, F. Finger, and E. A. Schiff, in *Amorphous and Nanocrystalline Silicon Science and Technology – 2004*, edited by G. Ganguly, M. Kondo, E. A. Schiff, R. Carius, and R. Biswas (Materials Research Society, Symposium Proc. Vol. 808, 2004), 109—114.

12. "Hole Drift-Mobility Measurements in Contemporary Amorphous Silicon," S. Dinca, G. Ganguly, Z. Lu, E. A. Schiff, V. Vlahos, C. R. Wronski, Q. Yuan, in *Amorphous and Nanocrystalline Silicon Based Films - 2003*, edited by J.R. Abelson, G. Ganguly, H. Matsumura, J. Robertson, E. A. Schiff (Materials Research Society Symposium Proceedings Vol. 762, Pittsburgh, 2003), pp. 345--350.

13. "Infrared Charge-Modulation Spectroscopy of Defects in Phosphorus Doped Amorphous Silicon," Kai Zhu, E. A. Schiff, and G. Ganguly, in *Amorphous and Heterogeneous Silicon-Based Films- 2002*, edited by J.R. Abelson, J.B. Boyce, J.D. Cohen, H. Matsumura, J. Robertson (Materials Research Society Symposium Proceedings Vol. 715, Pittsburgh, 2002), 301--306.

14. R.S. Crandall, *J. Appl. Phys.* **55,** 4418 (1984).

15. M. Hack, S. Guha, and W. den Boer, *Phys. Rev. B* **33**, 2512 (1986).

16. J. W. Park, R. J. Schwartz , J. L. Gray, and G. B. Turner, in *Proc. of the 19rd Photovoltaic Specialists Conference* (IEEE, New York, 1988), pp. 55-60.

17. H. Zhu, A. K. Kalkan, J. Hou, and S. J. Fonash, *AIP Conf. Proceedings* **462**, 309 (1999).

18. Schropp R E I and Zeman M, *Amorphous and Microcrystalline Silicon Solar Cells: Modeling Materials, and Device Technology*, Kluwer, Boston (1998).

19. U. Dutta and P. Chatterjee, *J. Appl. Phys.* **96**, 2261 (2004).

20. E. A. Schiff, *Solar Energy Materials and Solar Cells* **78**, 567-595 (2003).

21. Other parameters used in the calculations: $N_C = N_V = 5\text{x}10^{20}$ cm^{-3}, E_G = 1.8 eV, μ_n = 200 cm^2/Vs. See ref. [20].

22. Qing Gu, Qi Wang, Eric A. Schiff, Yuan-Min Li, and Charles T. Malone, *J. Appl. Phys.* **76**, 2310--2315 (1994).

23. S. Dinca, G. Ganguly, Z. Lu, E. A. Schiff, V. Vlahos, C. R. Wronski, Q. Yuan, in *Amorphous and Nanocrystalline Silicon Based Films – 2003*, edited by J.R. Abelson, G. Ganguly, H. Matsumura, J. Robertson, E. A. Schiff (Materials Research Society Symposium Proceedings Vol. 762, Pittsburgh, 2003), pp. 345--350.

24. M. Brinza, E. V. Emilianova, and G. J. Adriaenssens, *Phys. Rev. B* **71**, 115209 (2005).

25. M. Brinza, G. J. Adriaenssens, and P. Roca i Cabarrocas, Thin Solid Films **427**, 123 (2003).

26. S. Guha, in: R.A. Street (Ed.), Technology and Applications of Amorphous Silicon, Springer, Berlin, 1999, pp. 252–305. The light-soaking measurements in Fig. 6.24 of this paper were done under open-circuit conditions (private communication with S. Guha).

27. For historical reasons dating to the earliest days of dispersive transport measurements, μ_d is often defined $\mu_d = d^2 / V t_T$ (i.e. without the factor of 2 of eq. (3)). For consistency, in this paper we have recalculated published drift-mobilities that used this alternative definition.

28. H. Scher, M. F. Shlesinger, and J. T. Bendler, *Physics Today* **44** (1), 26 (1991).

29. Qi Wang, Homer Antoniadis, E. A. Schiff, and S. Guha, *Phys. Rev. B* **47**, 9435--9438 (1993).

30. For standard time-of-flight measurements, carriers have traversed half the sample's thickness at the transit-time, so $L = d/2$, and $L/E = d^2/2V$. Fig. 3 was prepared by estimating drift-mobilities at $L/E = 2\text{x}10^{-9}$ cm^2/V from the actual measurements of μ_d as a function of voltage.

31. T. Tiedje, in *Hydrogenated Amorphous Silicon vol 2*, edited by J. D. Joannopoulos and G. Lucovsky (New York: Springer 1984), pp 261–300.

32. M. Zeman, J.A. Willeman, L.L.A. Vosteen G., Tao, and W.J. Metselaar, *Solar Energy Materials and Solar Cells* **46**, 81 (1997).

33. K. Zhu, J. Yang, W. Wang, E. A. Schiff, J. Liang, and S. Guha, in *Amorphous and Nanocrystalline Silicon Based Films – 2003*, edited by J.R. Abelson, G. Ganguly, H. Matsumura, J. Robertson, E. A. Schiff (Materials Research Society Symp. Proc. Vol. 762, Pittsburgh, 2003), pp. 297--302.

34. G. Juska, J. Kocka, M. Viliunas, and K. Arlauskas, *J. Non-Cryst. Solids* **164-166**, 579 (1993).

35. P. Stradins, H. Fritzsche, P. Tzanetakis, and N. Kopidakis, in *Amorphous Silicon Technology - 1996*, edited by M. Hack, *et al* (Materials Research Society Symp. Proc. Vol. 420, Pittsburgh, 1996), p. 729.

36. X. Deng and E. A. Schiff, in *Handbook of Photovoltaic Science and Engineering*, Antonio Luque and Steven Hegedus, editors (John Wiley & Sons, Chichester, 2003), pp. 505 – 565. The present samples and calculations are for weakly reflecting, stainless steel back contacts (*R* about 0.2) and full solar illumination. Modeling shows that highly reflecting back contacts have a maximum in their power vs. thickness curve that is not seen with non-reflecting back contacts.

37. V. D. Mihailetchi, J. Wildeman, and P. W. M. Blom, *Phys. Rev. Lett.* **94**, 126602 (2005).

38. J. Yang, A. Banerjee, and S. Guha, *Appl. Phys. Lett.* **70**, 2975 (1997).

39. T. Tiedje, *Appl. Phys. Lett.* **40**, 627 (1982).

40. Q. Gu, Q. Wang, E. A. Schiff, Y.-M. Li, and C. T. Malone, *J. Appl. Phys.* **76**, 2310 (1994) and references therein.

41. K. Zhu, J. Yang, W. Wang, E. A. Schiff, J. Liang, and S. Guha, in *Amorphous and Nanocrystalline Silicon Based Films – 2003*, edited by J.R. Abelson, G. Ganguly, H. Matsumura, J. Robertson, E. A. Schiff (Materials Research Society Symposium Proceedings Vol. **762**, Pittsburgh, 2003), p. 297.

42. Actual calculations require the densities of valence and conduction bandtail traps $g_v^0 = 6\times 10^{21}$ and $g_c^0 = 1.6\times 10^{22}$ $cm^{-3}s^{-1}$, respectively. These are not independent parameters since we use the assumption that the bandedge lies within the bandtail [41,20]

43. J. M. Pearce, R. J. Koval, A. S. Ferlauto, R. W. Collins, C. R. Wronski, J. Yang and S. Guha, *Appl. Phys. Lett.* **77**, 19 (2000).

44. J.-H. Lyou, E. A. Schiff, S. Guha, and J. Yang, *Appl. Phys. Lett.* **78**, 1924 (2001).

45. G. D. Cody, T. Tiedje, B. Abeles, B. Brooks, and Y. Goldstein, *Phys. Rev. Lett.* **47**, 1480 (1982).

46. R. A. Street, J. Zesch, and M. J. Thompson, *Appl. Phys. Lett.* **43**, 672 (1983).

47. H. Fritzsche, in *Annual Review of Material Research Vol. 31* (Annual Reviews, Palo Alto, 2001), p. 47.

48. B. Yan, J. Yang, and S. Guha, *Appl. Phys. Lett.* **83**, 782 (2003).

49. J. Liang, E. A. Schiff, S. Guha, B. Yan, and J. Yang, in P. C. Taylor, *et al.*, ed. *Amorphous and Nanocrystalline Silicon Technology – 2005* (Mater. Res. Soc. Symp. Proc. Vol.), *in press.*

50. H. M. Branz, *Phys. Rev. B* **l59,** 5498 (1999).

51. M. Stutzmann, W. B. Jackson, and C. C. Tsai, *Phys. Rev. B* **32**, 23 (1985). We note in passing that the value for C_{SW} that we extract from this paper is much larger than the values obtained from later, but otherwise similar, experiments [52,53].

52. H. Park, J. Liu, and S. Wagner, *Appl. Phys. Lett.* **55**, 2658 (1989).

53. T. Unold, J. Hautala, and J. D. Cohen, *Phys. Rev. B* **50**, 16985 (1994).

54. P. Stradins, unpublished.

55. P. Tzanetakis, N. Kopidakis, M. Androulidaki, C. Kalpouzos, P. Stradins, and H. Fritzsche, *J. Non-Cryst. Solids* **198-200**, (1996).

56. See the recent review of H. Fritzsche, *Annu. Rev. Mater. Res. 2001* **31**, 47–79.

57. H. N. Gleskova, J. N. Bullock, and S. Wagner, *J. Non-Cryst. Solids* **164-166**, 183 (1993).

58 M. A. Green, K. Emery, D. L. King, Y. Hishikawa, andW. Warta, *Prog. Photovol.:Res. Appl.* **15**, 35-40 (2007).

59 M. A. Contreras, K. Ramanathan, J. AbuShama, F .Hasoon, D. L. Young, B. Egaas and R. Noufi, *Prog. Photovolt: Res. Appl*., **13**, 209 (2005).

60 M. Gloeckler, J. R. Sites, W. K.Metzgeger *J. Appl. Phys.,* **98**, 113704 (2005), W. K. Metzgeger, M. Gloeckler, *J. Appl. Phys.,* **98**, 063701 (2005)

61 D. J. Schroeder J. L. Hernandez, G. D. Berry, and A. A. Rockett, *J. Appl. Phys.,* **83**, 1519 (1998)

62 S. Siebentritt *Thin Solid Films* **480–481,** 312 (2005).

63 I. L. Repins, B. J. Stanbery, D. L. Young3 S. S. Li, W. K. Metzger, C. L. Perkins, W. N. Shafarman, M. E. Beck, L. Chen, V. K. Kapur, D. Tarrant, M. D. Gonzalez, D. G. Jensen, T. J. Anderson, X. Wang, L. L. Kerr, B. Keyes, S.Asher, A. Delahoy and B. Von Roedern, *Prog. Photovolt: Res. Appl*. **14**, 25 (2006).

64 JinWoo Lee, J. D. Cohen, W. N. Shafarman, *Thin Solid Films* **480–481**, 336 (2005).

65 M. A. Contreras, B. Egaas, K. Ramanathan, J. Hiltner, A. Swartzlander, F. Hasoon and R. Noufi, *Prog. Photovolt: Res. Appl*. **7**, 311 (1999).

66 W. N. Shafarman, R. Klenk, and B. E. McCandless *J. Appl. Phys*., **79,** 9 (1996)

67 A. Shah, J. Meier A.Buechel, U.Kroll, J.Steinhauser, F.Meillaud, H.Schade, Paper to be presented at the ICCG5 Conference in Saarbrücken (D), July 2004, *Thin Solid Films* **502**, 292 (2006).

68 R. A. Street, Appl. *Phys. Lett*. **41**, 1060 (1982).

69 R. A. Street, *Phs. Rev B* **27**, 4924 (1983).

70 K**.** Hecht, *Z. Physik* **77**, 235 (1932).

71 S. Fonash: "*Solar Cell Device Physics"* Wiley, (1982), p.24, H. J .Hovel: "*Semiconductors and Semimetals"*, Vol.**11**, p.50, edited by Willardson and Beer (Academic Press, New York 1975) .

72 Qi Wang, H. Antoniadis, E. A. Schiff, and S. Guha, *Phys. Rev. B* **47**, 9435 (1993).

73 I. Balberg, D. Albin, R. Noufi *Appl. Phys. Lett.* **54,** 1244 (1989).

74 S. M. Sze: "*Physics of Semiconductor Devices*", Wiley, (1998).

75 R. Walker and H. Wallman, in "*Vacuum. Tube Amplifiers"*, McGraw Hill, (1948).

76. N. Wyrsch, M. Goerlitzer, N. Beck, J. Meier, and A. Shah, in *"Amorphous Silicon Technology – 1996"*, edited by M. Hack, E. A. Schiff, S. Wagner, R. Schropp, and A. Matsuda (Materials Research Society Symposium Proceedings Vol. 420, Pittsburgh, 1996), p. 801.

77. G. Juška, M. Viliūnas, K. Arlauskas, N. Nekrašas, N. Wyrsch, and L. Feitknecht, *J. Appl. Phys.* **89**, 4971 (2001).

78. M. Serin, N. Harder, R. Carius, *Journal of Materials Science: Materials in Electronics* **14**, 733 (2003).

79. T. Dylla, F. Finger, E. A. Schiff, unpublished.

80. J. Meier, R. Flückiger, H. Keppner, and A. Shah, *Appl. Phys. Lett.* **65**, 860 (1994).

81. O. Vetterl, A. Dasgupta, A. Lambertz, H. Stiebig, F. Finger and H. Wagner, Materials Research Society Symposia Proceedings, 664 (2001), A25.8.

82. T. Tiedje, in *Hydrogenated Amorphous Silicon II*, edited by J. D. Joannopoulos and G. Lucovsky (Springer-Verlag, New York, 1984), pp. 261-300.

83. T. Weis, R. Lipperheide, U. Wille, and S. Brehme, *J. Appl. Phys.* **92**, 1411 (2002).

84. L. Houben, M. Luysberg, P. Hapke, R. Carius, F. Finger, and H. Wagner, *Phil. Mag. A* **77**, 1447 (1998).

85. $\mu_D \equiv d^2 / 2(V + V_{bi})t_T$, where d is the i-layer thickness, V the applied voltage, V_{bi} is a correction for the internal field, and t_T is the transit-time corresponding to a charge collection of 50%.

86. S. Dinca, G. Ganguly, Z. Lu, E. A. Schiff, V. Vlahos, C. R. Wronski, Q. Yuan, in *Amorphous and Nanocrystalline Silicon Based Films – 2003*, edited by J. R. Abelson, G. Ganguly, H. Matsumura, J. Robertson, E. A. Schiff (Materials Research Society Symposium Proceedings Vol. 762, Pittsburgh, 2003), 343**.**

87. Q. Gu, Q. Wang, E. A. Schiff, Y.-M. Li, and C. T. Malone, *J. Appl. Phys.* **76**, 2310--2315 (1994).

88. The concept of a "thermal velocity" $v_{th} = (2k_BT/m_e)^{1/2}$ is based on effective-mass theory, and has no meaning in other transport models.

89. The multiple-trapping model invokes a "transport edge" that most workers associate with Nevill Mott's "mobility-edge;" however, alternate views have been proposed, in particular "hopping only" and "potential fluctuation" models.

90. Q. Wang, H. Antoniadis, E. A. Schiff, and S. Guha, *Phys. Rev. B* **47**, 9435 (1993).

91. S. Reynolds, V. Smirnov, C. Main, R. Carius, and F. Finger, in *Amorphous and Nanocrystalline Silicon Based Films – 2003*, edited by J. R. Abelson, G. Ganguly, H. Matsumura, J. Robertson, E. A. Schiff (Materials Research Society Symposium Proceedings Vol. 762, Pittsburgh, 2003), 327.

92. H. Overhof and P. Thomas, *Electronic Transport in Hydrogenated Amorphous Semiconductors* (Springer, New York, 1989).

93. R. Atta-Fynn, P. Biswas, P. Ordejón, and D. A. Drabold, *Phys. Rev. B* **69**, 085207 (2004).

94. A. Yelon and B. Movaghar, *Phys. Rev. B* **65**, 077202 (2002); A. Yelon, B. Movaghar, and H. M. Branz, *Phys. Rev. B* **46**, 12244 (1992).

95. L. C. Chen, L.A.Hamel, A.Yelon, *J. Non-Cryst. Solids* **220**, 254 (1997).

96. Q. Gu, E. A. Schiff, J.-B. Chevrier and B. Equer, *Phys. Rev. B* **52**, pp. 5695 (1995).

97. E. L. Williams, G. E. Jabbour, Q. Wang, S. E. Shaheen, D. S. Ginley, and E. A. Schiff, *Appl. Phys. Lett.* **87** 223504 (2005).

98. Vignesh Gowrishankar, Shawn R. Scully, Michael D. McGehee, Qi Wang and Howard M. Branz, *Appl. Phys. Lett.* **89**, 252102 (2006).

99. A. R. Middya, in "Electroabsorption and Transport Measurements and Modeling Research in Amorphous Silicon Solar Cells," E. A. Schiff, A. R. Middya, J. Lyou, N. Kopidakis, S. Rane, P. Rao, Q. Yuan, and K. Zhu, Final Technical Report, 24 March 1998–15 August 2002 (National Technical Information Service, Document DE20031500360).

100.M. J. Sailor, E. J. Ginsburg, C. B. Gorman, A. Kumar, R. H. Grubbs, and N. S. Lewis, *Science* **249**, 1146 (1990).

101. M. Sebastiani, L, Di Gaspare, G. Capellini, C. Bittencourt, and F. Evangelisti, *Phys. Rev. Lett.* **75** 3352-3355 (1995) and references therein.

102. M. Schmidt, A. Schoepke, L. Korte, O. Milch, W. Fuhs, *J. Non-Cryst. Solids*, **338-340** 211-214 (2004).

103. Product 650013 from Sigma-Aldrich, Inc.; dispersion D1020 from Ormecon GmbH.

104.D.P. Halliday, J.M. Eggleston, P.N. Adams, I.A. Pentland and A.P. Monkman, *Synth. Met.*,**85** 1245 (1997). We estimated the thickness *d* of PANI film from optical transmittance measurements at 500 nm and the absorption coefficients reported in this paper.

105. T. Sawada, N. Terada, S. Tsuge, T. Baba, T. Takahama, K. Wakisaka, S. Tsuda, and S. Nakano, *Conference Record of the 24th Photovoltaic Specialists Conference: Vol. 2* (IEEE, 1994), p.1219.

106 S. J. Fonash, *Solar Cell Device Physics* (Wiley, 1981), p.181.

107. R. Bruggemann, M. Rojahn, and M. Rosch, Phys. Stat. Sol. (a) **166**, R11 (1998); H. Meiling and R. E. I. Schropp, Appl. Phys. Lett. **74**, 1012 (1999); E. J. Meijer, M. Matters, P. T. Herwig, D. M. DeLeeuw, and T. M. Klapwijk, Appl. Phys. Lett. **76**, 3433 (2000); J. H. Schön, Ch. Kloc, and B. Batlogg, Phys. Stat. Sol. (b) **121**, R4 (2000).

108. H. Overhof and P. Thomas, *Electronic Transport in Hydrogenated Amorphous Semiconductors* (Springer, Berlin, 1989).

109. L. Bozano, S. A. Carter, J. C. Scott, G. G. Malliaras, and P. J. Brock, Appl. Phys. Lett. **74**, 1132 (1999).

110. J. Liang, E. A. Schiff, S. Guha, B. Yan, and E. A. Schiff, *Appl. Phys. Lett.* **88,** 063512 (2006).

111. R. M. A. Dawson, S. S. Nag, C. R. Wronski and N. Maley, *Conference Record of the Twenty Third IEEE Photovoltaic Specialists Conference, 1993*, pp. 960-965 (1993).

112. J. H. Lyou, E. A. Schiff, S. S. Hegedus, S. Guha, J. Yang, in Amorphous and Heterogeneous Silicon Thin Films: Fundamentals to Devices – 1999, edited by H. M. Branz, R. W. Collins, H. Okamoto, S. Guha, and R. Schropp (Materials Research Society, Symposium Proceedings Vol. 557, 1999), 457.

113. J. Lyou, N. Kopidakis, E. A. Schiff, *J. Non-Cryst. Solids* **266-269** (2000) 227.

114. K. Zhu, J. H. Lyou, E. A. Schiff, R. S. Crandall, G. Ganguly, S. S. Hegedus, Conference Record of the 28th IEEE Photovoltaics Specialists Conference (Institute of Electrical and Electronics Engineers, Inc., Piscataway, 2000) 725.

115. K. Zhu, E. A. Schiff, and G. Ganguly, *J. Non-Cryst. Solids*. in press (2002).

116. G. Weiser, U. Dersch, and P. Thomas, *Phil. Mag. B* **57**, 721 (1988).

117. K. Zhu, E. A. Schiff, and G. Ganguly, in *Amorphous and Heterogeneous Silicon-Based Films-2002,* edited by J. D. Cohen, J. R. Abelson, H. Matsumura, and J. Robertson (Materials Research Society, Symposium Proceedings vol. 715, Pittsburgh, 2002), 302.

118. M. P. Petkov, M. H. Weber, K. G. Lynn, R. S. Crandall, V. J. Ghosh, *Phys. Rev. Lett.* **82**, 3819 (1999).

119. R. A. Street, *Hydrogenated Amorphous Silicon* (Cambridge University Press, Cambridge, 1991).

REPORT DOCUMENTATION PAGE

Form Approved
OMB No. 0704-0188

The public reporting burden for this collection of information is estimated to average 1 hour per response, including the time for reviewing instructions, searching existing data sources, gathering and maintaining the data needed, and completing and reviewing the collection of information. Send comments regarding this burden estimate or any other aspect of this collection of information, including suggestions for reducing the burden, to Department of Defense, Executive Services and Communications Directorate (0704-0188). Respondents should be aware that notwithstanding any other provision of law, no person shall be subject to any penalty for failing to comply with a collection of information if it does not display a currently valid OMB control number.

PLEASE DO NOT RETURN YOUR FORM TO THE ABOVE ORGANIZATION.

1. REPORT DATE *(DD-MM-YYYY)*	2. REPORT TYPE	3. DATES COVERED *(From - To)*
October 2008	Subcontract Report	11 February 2002 – 30 September 2006

4. TITLE AND SUBTITLE
Transport, Interfaces, and Modeling in Amorphous Silicon Based Solar Cells: Final Technical Report, 11 February 2002 - 30 September 2006

5a. CONTRACT NUMBER
DE-AC36-99-GO10337

5b. GRANT NUMBER

5c. PROGRAM ELEMENT NUMBER

6. AUTHOR(S)
E.A. Schiff

5d. PROJECT NUMBER
NREL/SR-520-44101

5e. TASK NUMBER
PVB75401

5f. WORK UNIT NUMBER

7. PERFORMING ORGANIZATION NAME(S) AND ADDRESS(ES)
Syracuse University
Syracuse, New York 13244

8. PERFORMING ORGANIZATION REPORT NUMBER
NDJ-2-30630-24

9. SPONSORING/MONITORING AGENCY NAME(S) AND ADDRESS(ES)
National Renewable Energy Laboratory
1617 Cole Blvd.
Golden, CO 80401-3393

10. SPONSOR/MONITOR'S ACRONYM(S)
NREL

11. SPONSORING/MONITORING AGENCY REPORT NUMBER
NREL/SR-520-44101

12. DISTRIBUTION AVAILABILITY STATEMENT
National Technical Information Service
U.S. Department of Commerce
5285 Port Royal Road
Springfield, VA 22161

13. SUPPLEMENTARY NOTES
NREL Technical Monitor: Bolko von Roedern

14. ABSTRACT *(Maximum 200 Words)*
In this report, we present the results for the four principal tasks of this research project: 1. Amorphous silicon solar cell characteristics and modeling; 2. Photocarrier drift mobility measurements in hydrogenated amorphous silicon, microcrystalline silicon, and polycrystalline copper indium-gallium diselenide; 3. Hole-conducting polymers as *p*-layer materials for amorphous and crystal silicon solar cells; and 4. Infrared spectra of *p/i* and *n/i* interfaces in a-Si:H-based solar cells.

15. SUBJECT TERMS
PV; solar cells; amorphous silicon; microcrystalline silicon; CIGS; drift mobility; polymers; infrared spectra

16. SECURITY CLASSIFICATION OF:			17. LIMITATION OF ABSTRACT	18. NUMBER OF PAGES	19a. NAME OF RESPONSIBLE PERSON
a. REPORT	b. ABSTRACT	c. THIS PAGE			
Unclassified	Unclassified	Unclassified	UL		19b. TELEPHONE NUMBER *(Include area code)*

Standard Form 298 (Rev. 8/98)
Prescribed by ANSI Std. Z39.18

F1146-E(09/2007)